*Geophys. J. Int.* (2002) **148,** 476–498

# Adaptive wavelet-based finite-difference modelling of *SH*-wave propagation

Stéphane Operto, Jean Virieux, Bernhard Hustedt and Fabrizio Malfanti

*UMR Géosciences Azur, CNRS, UNSA, UPMC, France. E-mail: operto@obs-vlfr.fr, viri@geoazur.unice.fr, hustedt@geoazur.unice.fr*

Accepted 2001 August 7. Received 2001 June 7; in original form 2000 December 4

## SUMMARY

An adaptive wavelet-based finite-difference method for 2-D *SH*-wave propagation modelling is presented. The discrete orthogonal wavelet transform allows the decomposition of spatial wavefield coordinates on to different grids of various resolution. At different times during propagation and locations in the model, the different scales involved in the decomposition give different contributions to the wavefield construction. The orthogonal wavelet basis provides a natural framework to adapt spatial grids to local wavefield properties in time and space. In this paper, the efficiency of this approach is assessed in terms of computational cost and accuracy for different 2-D heterogeneous media.

The classic $\mathcal{O}(\Delta t^2, \Delta x^4)$ time–space finite-difference method is recast into the time–spatial-wavelet domain. Wavefields, spatial differential and medium convolution operators are decomposed on to spatial orthogonal wavelet bases. These spatial operators may be applied in the wavelet domain or may be applied by going back and forth in the spatial domain. These two strategies provide similar results but differ in efficiency. Then, wavelet coefficients are extrapolated in time through second-order differencing using a constant time step. Recomposition in the original spatial domain may be performed for analysis of the results. Wavelet implementations of source excitation, PML-like absorbing boundary conditions and a free surface have also been implemented and are described for realistic wave propagation using the wavelet approach.

Contrasted and structurally complex heterogeneous models such as the corner–edge and Marmousi models are considered for a comparison with the staggered-grid time–space finite-difference method. The numerical results compared well with those of time–space finite-difference method provided that sharp variations in the medium and the wavefields can be oversampled in the finest grid of the multiresolution analysis. In the smooth parts of the medium, a rule of thumb of five nodes per wavelength is used for the wavelet approach as for the $\mathcal{O}(\Delta t^2, \Delta x^4)$ standard finite-difference methods. Nevertheless, the discretization is adapted to the local wavelength in the wavelet approach, while the unique discretization involved in the standard finite-difference method is matched to the minimum wavelength.

An accurate presentation of the efficiency of the method is difficult because interpolations are not identical to those used in staggered-grid time–space finite-differences approaches and because the multiresolution analysis provides a complementary discretization of the medium, which may affect the numerical results without any corresponding effect in the standard approach. Actually, the wavelet approach in its different forms requires much greater computer resources than standard approaches. A future implementation of the time adaptivity with the time step being adapted to the local grid resolution of the multiresolution analysis will improve the CPU efficiency and will enhance the accuracy of the method by limiting the grid dispersion.

Despite its present CPU limitations, the wavelet method provides a new flexible numerical tool to adapt wave phenomena discretization to local media properties. This flexibility is invaluable and could be important when complex boundary interactions and non-linear rheology of near-surface models are treated.

**Key words:** finite-difference methods, multiresolution analysis, spatial adaptivity, wave modelling, wavelet, transform.

## 1 INTRODUCTION

Finite-difference (FD) methods enjoy considerable popularity in the field of geophysics for 2-D and 3-D seismic wave propagation modelling (e.g. Kelly *et al.* 1976; Virieux 1984; Levander 1988; Graves 1996). These methods are attractive because of their relatively straightforward implementation and their reliability for structurally complex media. The main drawback is their heavy computational cost. Indeed, the classic FD formulation requires a uniform wavefield discretization in time and space. This can be expensive in terms of computing time, especially in 3-D heterogeneous elastic media where contrasted wavelengths may occur in the modelling (e.g. velocities may range between 0.2 km $s^{-1}$ for the lowest *S*-wave velocity and 8.2 km $s^{-1}$ for the highest *P*-wave velocity for an elastic crustal model). Numerical forward modelling of seismic wave propagation has been improved recently by taking into account more sophisticated mesh structures (Aoi & Fujiwara 1999; Mozco *et al.* 1999; Hestholm 1999; Komatitsch & Tromp 1999; Pitarka 1999) rather than standard cartesian regular grids. By doing so, finite-difference methods borrow some well-known features, such as mesh generation, from finite-element methods (Day 1982). The number of numerical operations required in computing partial differential operators while handling the irregular node distribution increases sligthly. On the other hand, optimal minimum meshes may be designed for a required precision of wave propagation (Magnier *et al.* 1994).

Mesh generation (Sambridge *et al.* 1995) will be a key step in the simulation performance and different strategies exist to design these grids before computation starts. For example, one should increase the number of nodes in areas of strong velocity variation. If, by mistake, the mesh is not designed properly, the accuracy of the wave propagation simulation will decrease dramatically. Moreover, the user will be unable to detect it. Nowadays, multigrids or unstructured grid constructions are starting to be very popular for wave propagation simulations (Berger & Oliger 1984; Magnier *et al.* 1994; Dormy & Tarantola 1995; Berger & LeVeque 1998).

Another direction, based on adaptive mesh design as the wave propagates, is worth investigating (e.g. Joly *et al.* 1994; Biswas *et al.* 1993; Lazaar *et al.* 1994; Charton 1996) and we shall focus on such an approach in this paper.

The simulated wavefield is decomposed on to different grids of various resolution. Wavefields are constructed on each grid at each time step of the simulation. The final wavefield, namely the wavefield integrating all resolutions, is obtained by summing up wavefield contributions from each grid. The adaptivity results from the restriction of wavefields on each grid over time evolution.

Different decompositions exists, though the discrete orthogonal wavelet transform provides a natural tool that nicely introduces the scale decomposition we are interested in (Mallat 1989; Mallat 1999). The discrete forward wavelet transform initially discretizes a signal on to a fine grid and subsequently finds its decomposition on to a hierarchy of finite-difference grids of decreasing resolution. Each grid of the multiresolution decomposition encodes the increment of information that is lost when the projection of the signal at a given resolution is projected on to the next coarser resolution grid. This increment of information is represented by the so-called wavelet coefficients. The projection of the signal on the coarsest grid of the decomposition is stored in addition to the wavelet coefficients associated with each grid in order to reconstruct the initial signal. This cascade of projections followed by subsampling, called multiresolution analysis, allows the design of a non-redundant (orthogonal) transform. The discrete inverse wavelet transform is computed by proceeding in the opposite direction, namely, from coarse to fine scales.

In this paper, we describe the basic steps of such an approach using the 2-D explicit velocity–stress finite-difference method of Virieux (1984) in the time–spatial-wavelet domain. Time derivatives are discretized using the standard centred finite-difference scheme. Spatial wavefield coordinates and differential operators are decomposed into a wavelet basis. Our motivation for using spatial wavelet decompositions is driven by possible mesh spacing optimizations during time evolution. The spatial finite-difference grids are adapted with respect to local wavefield properties. This optimization can be achieved through an analysis of the amplitude of wavelet coefficients that represent the discretized wavelet-transformed wavefields. If local wavefield properties (e.g. the local wavelength) do not require a fine discretization, it is expected that the wavelet coefficients associated with the fine grids will have low amplitudes. Therefore, there is no need to propagate them. We call this procedure space adaptivity. During time evolution, the spatial finite-difference grids are locally adapted with respect to wavefield properties.

Further optimization may be obtained when time adaptivity is implemented. During the time extrapolation, time steps are adapted to each spatial finite-difference grid. This has been proposed by Tessmer (2000) for standard finite-difference approaches.

We have not implemented time adaptivity as yet. It appears not to be straightforward (Bacry *et al.* 1992) owing to coupling between different scales when an operator such as the differential operator is applied to the wavefield.

Different attempts have been performed previously using wavelet-based wave simulations with rather simple model configurations (Bacry *et al.* 1992; Joly *et al.* 1995; Wu & McMechan 1998). We present both quantitative comparisons with analytical solution for simple models and an analysis of wavelet effects for contrasted and structurally complex heterogeneous media. We show that our wavelet approach gives correct results for these simulations although an objective presentation of the efficiency of the method compared with standard time–space finite-difference methods could not be performed here. In the proposed examples, either coupled grids required additional operations or necessary medium convolutions handicaped the performance. Moreover, we show that the explicit projection of the differential operator in the wavelet basis does not lead to a discretization of the wavefields on staggered grids. Despite these present limitations, the time–wavelet method may be of interest for specific applications.

For example, accurate boundary conditions can generally be verified by oversampling the discrete problem in the vicinity of the boundary. Compared with the time–space method, the time–wavelet method may increase the computational speed by limiting the area of the oversampling to just in the vicinity of the boundary. This can be achieved by forcing to zero the fine grid nodes located outside a local area centred on the boundary (i.e. by applying a mask). Typically, such a boundary condition could be applied to the free surface in the presence of topography.

Moreover, the automatic multigrid decomposition provided by the wavelet transform may easily handle the particular case

where the geometry of the boundary varies with time. In this case, the mesh refinement must be performed dynamically during the simulation. An example of such an application is the seismic rupture problem that involves a curved fault or several fault segments, the geometries of which evolve in time. For this dynamic case, the wavelet transform will perform well because the multigrid decomposition associated with the wavelet transform is easy to compute, automate and then can be adapted over time. This is not the case with other multigrid or finite-element methods based on unstructured grids where the unique mesh is generated before the simulations start. This topic will be addressed in a future paper.

A third application is modelling of non-linear wave phenomena associated with complex rheology. Again these phenomena may occur locally in a weathered layer located near the surface.

This paper is divided into three principal sections. In the first part, we introduce the physical concepts underlying multiresolution analysis and discrete wavelet transform (Mallat 1989, 1999; Daubechies 1992). These physical concepts are illustrated within the framework of a wave propagation modelling problem. In Appendix A, we review the derivation of the differential operator in the wavelet basis and its connection with the classic finite-difference approximation of the differential operator (Beylkin 1992; Jameson 1993). Then, we analyse the convolution of the differential operator in a wavelet basis with heterogeneous medium properties. They are required for the formulation of the *SH* velocity–stress system of equations in the wavelet domain. We describe the practical implementation of source excitation and a free surface in the wavelet domain. Then, we present an analysis of source excitation in the wavelet domain. In the case of an impulsive point source, we observed numerical artefacts. These are caused by the finite-difference stencils of the derivative operator in the wavelet basis. We show that these stencils do not lead to a representation of wavefields on staggered grids. Since finite-difference grids are always bounded, we propose an efficient absorbing boundary condition in the wavelet domain based on the perfectly matched layer (PML) approach (Berenger 1994). In the second part, we clarify the necessary numerical operations for wave simulations in the wavelet domain and discuss the main aspects of our implementations. In the third part, different numerical examples from simple models to rather complex ones such as the Marmousi model (Bourgeois *et al.* 1991) will illustrate properties of this so-called adaptive time wavelet finite-difference formulation. The performance of our method will be assessed by comparison with the classic staggered-grid time–space finite-difference method (Virieux 1984). Furthermore, we discuss present limitations of such an approach and potential perspectives one may hope to reach in the future.

## 2 WAVELET-BASED MODELLING OF *SH*-WAVE PROPAGATION

### 2.1 Multiresolution analysis and wavelet transform of a 2-D wavefield

In this section, we illustrate the basic physical principle underlying multiresolution analysis and wavelet transform with a wave propagation example. We refer the reader to the original papers and textbooks of Daubechies (1988), Mallat (1999); Mallat (1989) and Daubechies (1992) for rigorous mathematical developments.

Let us consider a continuous wavefield $f(x, z)$ for an explosive source in a 2-D homogeneous medium. In a 2-D discrete space defined as the domain $\mathbf{V}_0 \times \mathbf{V}_0$, a snapshot of the wavefield is shown in Fig. 1(a). The wavefield was emitted by a spatially smoothed point source and was subsequently propagated in a 4 km $s^{-1}$ homogeneous medium. The source bandwidth has a maximum frequency of 20 Hz. The number of grid points in $V_0$ was 256, the mesh spacing $h_0$ was 40 m. The approximation of the continuous wavefield on this discrete domain will be denoted by $P_{\mathbf{V}_0 \times \mathbf{V}_0} f(x, z)$. It represents the discrete wavefield that may be obtained with a classic time–space finite-difference method. Let us assume that $f(x, z)$ can be approximated by $P_{\mathbf{V}_0 \times \mathbf{V}_0} f(x, z)$ provided that a sufficiently fine discretization of $\mathbf{V}_0$ has been defined.

The 2-D orthogonal wavelet transform of the discrete wavefield will cascade orthogonal projections of this snapshot over different approximation grids $\mathbf{V}_1, \mathbf{V}_2, \ldots, \mathbf{V}_J$ of decreasing resolution for each spatial dimension $x$ and $z$ (similarly to the Fourier transform, a 2-D wavelet transform can be computed by applying sequentially a 1-D transform on each dimension). Generally, the resolution of each suddomain $\mathbf{V}_j$ decreases by a factor of 2 from one subdomain to the next. This implies that $h_{j+1} = 2h_j$ where $h_{j+1}$ and $h_j$ denote the mesh spacing in the $\mathbf{V}_{j+1}$ and $\mathbf{V}_j$ grids, respectively. An orthonormal basis of $\mathbf{V}_j$, $\{\phi_{j,n}\}_{n \in N}$, can be formed by dilating and translating a single function $\{\phi_n\}_{n \in N}$, the scaling function.

$$\phi_{j,n}(x) = 2^{-j/2}\, \phi\left(2^{-j} x - n\right) \tag{1}$$

At each step of the cascade, the wavelet transform also encodes the increment of information that is lost when the wavefield at a given resolution $j$ is projected on to a subdomain of twice as coarse resolution, $j+1$. This increment of information is obtained by orthogonal projection of the wavefield over the complementary domain $\mathbf{W}_{j+1}$ of $\mathbf{V}_{j+1}$, $\mathbf{V}_j = \mathbf{W}_{j+1} \oplus \mathbf{V}_{j+1}$. The orthonormal basis of $\mathbf{W}_j$, $\{\psi_{j,n}\}_{n \in N}$, is also formed by dilating and translating a single function $\{\psi_n\}_{n \in N}$, the wavelet function,

$$\psi_{j,n}(x) = 2^{-j/2}\, \psi\left(2^{-j} x - n\right). \tag{2}$$

The wavelet and scaling functions are related by quadrature mirror filters,

$$\begin{aligned} \phi(x) &= \sqrt{2} \sum_{n=-\infty}^{\infty} h[n]\phi(2x - n) \\ \psi(x) &= \sqrt{2} \sum_{n=-\infty}^{\infty} g[n]\phi(2x - n), \end{aligned} \tag{3}$$

where $g[n] = (-1)^{1-n} h[1-n]$.

The increment of information in $\mathbf{W}_{j+1}$ is discretized by the so-called wavelet coefficients, $\{d_{j+1,n}\}_{n \in N}$, while the projection of the signal on to the approximation spaces $\mathbf{V}_{j+1}$ is discretized by the so-called scaling coefficients, $\{s_{j+1,n}\}_{n \in N}$. In order to design an orthogonal transform (i.e. non-redundant transform), at each step of the cascade the scaling coefficients of the subdomain $\mathbf{V}_j$ are replaced by the wavelet coefficients of the subdomain $\mathbf{W}_{j+1}$ and the scaling coefficients of the subdomain $\mathbf{V}_{j+1}$. This procedure is iterated up to the coarsest approximation space $\mathbf{V}_J$ of the multiresolution analysis. Indeed, at the last iteration of the procedure, both wavelet and scaling coefficients of subdomains $\mathbf{W}_J$ and $\mathbf{V}_J$ are kept in order to be able to reconstruct the wavefield in the original domain $\mathbf{V}_0 \times \mathbf{V}_0$ by reversing the procedure. Finally, a 1-D signal $f$ can be

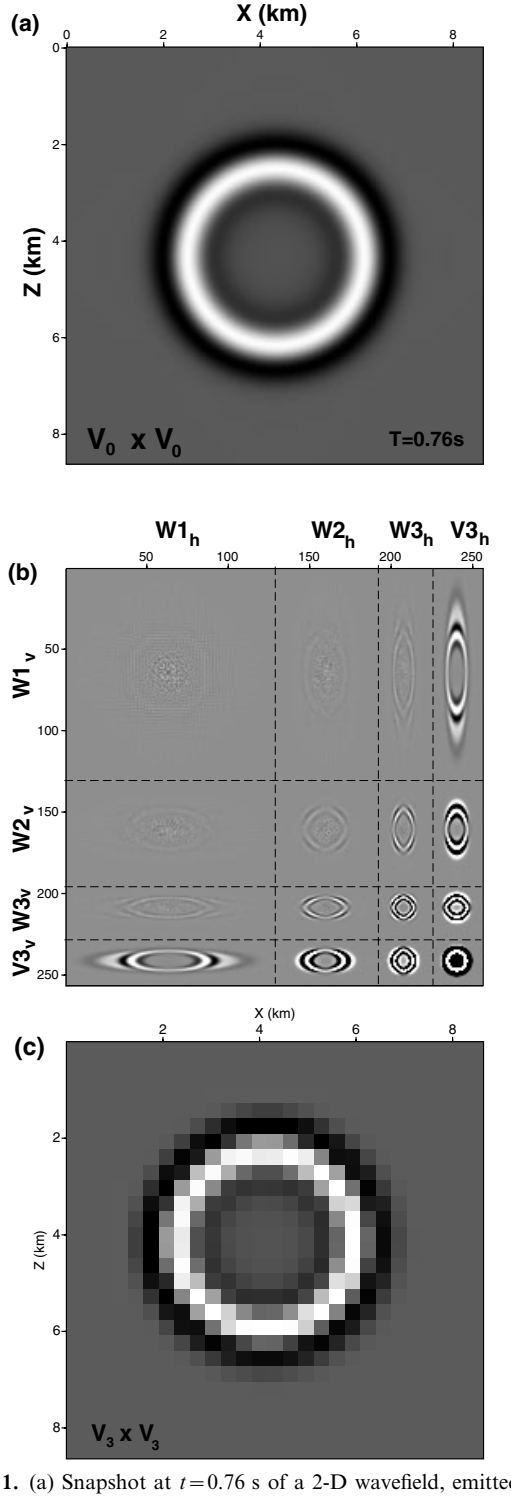


**Figure 1.** (a) Snapshot at $t=0.76$ s of a 2-D wavefield, emitted by a smoothed point source that propagates in a homogeneous medium with velocity 4 km s$^{-1}$ and density 2.5 g cm$^{-3}$. The wavefield is represented in the $\mathbf{V}_0$ space of the multiresolution analysis. The figure is discretized with $256 \times 256$ nodes and a mesh spacing of 40 m. (b) The same wavefield as in Fig. 1(a) but plotted in the wavelet domain. The decomposition was computed over three resolutions. The axes are labelled with sample numbers discretizing the image. $\mathbf{W}_h$ and $\mathbf{V}_h$, $\mathbf{W}_v$ and $\mathbf{V}_v$, label the wavelet and scaling subspaces of the multiresolution analysis on the horizontal, vertical direction, respectively. (c) Close-up of Fig. 1(b) corresponding to the approximation subspace $\mathbf{V}_{3_h} \times \mathbf{V}_{3_v}$. This picture is discretized with $32 \times 32$ nodes and mesh spacing of 160 m. The same spatial domain is mapped but with a different resolution.

decomposed on to a 1-D wavelet basis as

$$f(x) = \sum_{j=1}^{J} \sum_{n=-\infty}^{+\infty} \langle f(x), \psi_{j,n}(x) \rangle \psi_{j,n}(x) + \sum_{n=-\infty}^{+\infty} \langle f(x), \phi_{J,n}(x) \rangle \phi_{J,n}(x) \,. \tag{4}$$

The fast wavelet transform computed over the scales 1 to $J$ will replace the discrete values of $f$ in $\mathbf{V}_0$ by the wavelet coefficients $\{d_{j,n}\}_{\substack{j=1,J \\ n \in N}} = \{\langle f, \psi_{j,n} \rangle\}_{\substack{j=1,J \\ n \in N}}$ and the scaling coefficients $\{s_{J,n}\}_{n \in N} = \{\langle f, \phi_{J,n} \rangle\}_{n \in N}$. As for the fast Fourier transform, the successive subdivisions of the data by a factor of 2 in the fast wavelet transform algorithm require that the number of samples in $f$ is an integer power of 2. This will make our implementation of the time–wavelet finite-difference method less flexible than the classic time–space finite-difference method. Nevertheless, recent wavelet transform algorithms that do not even require a regular grid may allow one to design more general finite-difference modelling algorithms in the future (Sweldens 1997). An easy-to-read description of the fast wavelet transform algorithm can be found in Press *et al.* (1992, pp. 584–599). As mentioned before, a 2-D orthogonal wavelet transform can be computed by applying sequentially a 1-D transform on each dimension. This illustrates the natural property of the tensor product construction of 1-D wavelet bases. A 2-D signal $f(x, z)$ can be decomposed on to a 2-D wavelet basis as

$$\begin{aligned} f(x,z) = & \sum_{j=1}^{J} \sum_{n=-\infty}^{+\infty} \sum_{l=1}^{L} \sum_{m=-\infty}^{+\infty} \langle f(x,z), \psi_{j,n}(x)\psi_{l,m}(z) \rangle \psi_{j,n}(x)\psi_{l,m}(z) \\ & + \sum_{j=1}^{J} \sum_{n=-\infty}^{+\infty} \sum_{m=-\infty}^{+\infty} \langle f(x,z), \psi_{j,n}(x)\phi_{L,m}(z) \rangle \psi_{j,n}(x)\phi_{L,m}(z) \\ & + \sum_{n=-\infty}^{+\infty} \sum_{l=1}^{L} \sum_{m=-\infty}^{+\infty} \langle f(x,z), \phi_{J,n}(x)\psi_{l,m}(z) \rangle \phi_{J,n}(x)\psi_{l,m}(z) \\ & + \sum_{n=-\infty}^{+\infty} \sum_{m=-\infty}^{+\infty} \langle f(x,z), \phi_{J,n}(x)\phi_{L,m}(z) \rangle \phi_{J,n}(x)\phi_{L,m}(z) \,. \end{aligned} \tag{5}$$

In eq. (5), the decomposition was computed over $J$ and $L$ scales for the $x$ and $z$ dimensions, respectively. The indices $j$ and $l$ are the dilation indices for the $x$ and $z$ dimensions, respectively, $n$ and $m$ are the translation indices for the $x$ and $z$ dimensions, respectively. The same wavefield as that of Fig. 1(a) is shown in Fig. 1(b), though now after a 2-D wavelet transform over three approximation spaces $\mathbf{V}_1$, $\mathbf{V}_2$ and $\mathbf{V}_3$.

Although the wavefield is represented at different scales in Fig. 1(b), the total description requires the same number of nodes as the initial one in Fig. 1(a), namely $256 \times 256$. This illustrates the non-redundancy (i.e. orthogonality) of the wavelet transform used.

The image is subdivided into different 2-D subdomains $(\mathbf{W}_{i_h} \times \mathbf{W}_{j_v}, \mathbf{W}_{i_h} \times \mathbf{V}_{3_v}, \mathbf{V}_{3_h} \times \mathbf{W}_{j_v})_{i,j=1,3}$ delineated by the dashed lines. They are discretized by the coefficients of eq. (5) for $j=1$, 3 and $l=1$, 3 (subscripts h and v label the horizontal and vertical scales, respectively). The spatial size of each subdomain is the same as in Fig. 1(a). Horizontal and vertical discretizations are matched to the resolution of the associated approximation

spaces $\mathbf{V}_j$ (e.g. the subdomain $\mathbf{W}_{1_h} \times \mathbf{W}_{2_v}$ is discretized with a horizontal and vertical mesh spacing of 80 m and 160 m, respectively). According to eqs (1) and (2), the mesh spacing increases by a factor of 2 from scale $j$ to $j+1$. Note that the decay of the wavelet coefficient amplitude across scales. This illustrates the local regularity of the wavefield (Mallat 1999, pp. 169–171). Fig. 1(c) shows a close-up of Fig. 1(b). The image is centred on the coarsest approximation subspace $\mathbf{V}_3$, i.e. it is discretized on to a $64 \times 64$ grid with 320 m mesh spacing.

### 2.2 The differential operator in the Daubechies-4 wavelet basis

In this paper, we have used the compactly supported wavelet basis of Daubechies with two vanishing moments (Daubechies-4 wavelets) (Daubechies 1992). The discrete wavelet transform was computed applying algorithms provided in Press *et al.* (1992, p. 595). We selected this basis for two main reasons: first, the local wavelet support allows fast transform computations (the quadrature mirror filters $h$ and $g$, eq. (3), associated with the Daubechies-4 wavelets are represented by four coefficients only) (Daubechies 1992; Press *et al.* 1992). Second, there is a close relationship between the representation of the differential operator in the Daubechies wavelet basis and the finite-difference approximation of the differential operator in the physical domain (Beylkin 1992; Jameson 1993).

In this study, we have computed the projection of the differential operator explicitly in the Daubechies-4 wavelet basis from the definition of the scaling and wavelet interpolating functions (Beylkin 1992 and Appendix A). Alternatively, one can define a finite-difference approximation of the differential operator in the $\mathbf{V}_0$ grid (independently from the properties of the wavelet interpolating functions) and then compute its wavelet transform (Wu & McMechan 1998). In the case of the Daubechies-4 wavelets, these two procedures are equivalent if the differential operator is discretized in the $\mathbf{V}_0$ grid with central finite-difference stencils of coefficients ($-1/12$, 2/3, 0, $-2/3$, 1/12). Then, the projection of the differential operator on the Daubechies 4-wavelet basis is equivalent to a fourth-order central finite-difference differential operator (Beylkin 1992; Jameson 1993) (see Appendix A for details).

More generally, the projection of the differential operator in a Daubechies wavelet basis with $M$ vanishing moments has the same properties as a finite-difference derivative operator of order $2M$ (Jameson 1993). Note that wavelet properties do not naturally lead to staggered grid finite-difference stencils. Indeed, for staggered grids the fourth-order finite-difference stencils do not have a zero central coefficient. Staggered grid finite-difference stencils proposed by Levander (1988) have coefficients of (1/24, $-9/8$, 9/8, $-1/24$). We will show that the implementation of standard and staggered grids in the time–wavelet and time–space algorithms, respectively, induces different results between the two methods. Clearly, the wavelet transform is not directly responsible for such different results. These differences are related to numerical dispersion and noise occurring in the time–wavelet formulation. Still, we will propose a strategy that takes advantage of the multigrid decomposition to avoid the unwanted artefacts (see Section 2.4). Therefore, we shall be able to compare quantitatively our numerical simulations with results of the $\mathcal{O}(\Delta t^2, \Delta x^4)$ time–space and $\mathcal{O}(\Delta t^2$, Daubechies-4) time–wavelet FD methods. We stress that the computer efficiency analysis is still beyond our control. Another criteria to select a wavelet basis among all available bases would be their efficiency in compressing the wavefield. We have not addressed this problem yet.

### 2.3 Convolution by heterogeneous medium properties

Spatial partial differential values of a given wavefield $f(x, z, t)$ need to be estimated in the wavelet domain where the wave equation has to be solved. In any heterogeneous medium, one more step is required. The obtained field $\partial f(x, z, t)/\partial x$ subsequently has to be convolved with one of the medium properties $g(x, z)$ (the shear modulus and the buoyancy in the *SH* case). In the physical domain, this is a simple spatial product

$$g(x, z) \frac{\partial f(x, z, t)}{\partial x} . \tag{6}$$

This product is transformed using a convolution procedure in the wavelet domain (see eq. 8 below). This convolution is quite demanding in terms of computer resources.

A simple implementation is the local homogeneity approximation as tested by Wu & McMechan (1998). In their approach, the function $g(x, z)$ is locally replaced by a homogeneous value $g_0$. In fact, this well-known strategy of standard finite-difference methods (Boore 1972) has been found to be a rather crude approximation which is only valid in very smooth heterogeneous media.

We prefer to compute this convolution through two different strategies. Both strategies depend significantly on the performance of the fast wavelet transform. The first approach follows the same lines as the Fourier method proposed by Kosloff & Baysal (1982). In order to estimate a partial derivative, they estimate the Fourier transform of the field, compute the derivative in the Fourier domain by a simple multiplication and return to the standard space for integration of equations. When the Fourier transform is fast, this derivative estimation is efficient and it is very accurate as well. We apply the same approach for our specific need: we come back to the standard space for multiplication of eq. (6) and return immediately to the wavelet space for time integration. We call this approach the time pseudo-wavelet finite-difference approach, hereafter denoted as the TPWFD formulation. This approach requires only the storage of medium properties in the $\mathbf{V}_0$ domain (discretized on an $nx \times nz$ grid) and the storage of the partial differential operator in the wavelet domain with respect to the $x$- and $z$-coordinates (see Appendix A). These operators are discretized with $nx \times nx$ and $nz \times nz$ square matrices for the $x$- and $z$-dimensions, respectively.

The second approach estimates the product explicity in the wavelet domain. By doing so, an additional effort is required that limits the efficiency of the method. We call this approach the time wavelet finite-difference approach, hereafter denoted as the TWFD formulation. For the convolution estimation, we write the wavelet decomposition of the function $f(x, z, t)$ through the tensorial expression in compact form

$$f(x, z, t) = \sum_i \sum_l \langle f(x, z, t), \Psi_i(x)\Psi_l(z) \rangle \Psi_i(x)\Psi_l(z) , \tag{7}$$

where functions $\Psi_i$ and $\Psi_l$ denote the wavelet and scaling functions $\psi$ and $\phi$, equations 1 and 2. The indices $i$ and $l$ represent translation and dilation factors for the $x$ and $z$ coordinates, respectively. The coefficients $\langle f, \Psi_i \Psi_l \rangle$, associated with the basis functions $\Psi_i$ and $\Psi_l$, are computed using 2-D discrete wavelet transform (e.g. Press *et al.* 1992). The 2-D wavelet coefficients of the product of the function $g$ with the partial derivative of the function $f$ may be computed as follows (see Appendix B for details):

$$\begin{aligned}\left\langle g(x,z)\,\frac{\partial f(x,z,t)}{\partial x},\,\Psi_i(x)\Psi_l(z)\right\rangle &= -\sum_j\sum_k\left\langle \Psi_j(x),\,\frac{\partial \Psi_k(x)}{\partial x}\right\rangle \\ &\quad\times\sum_m\left\langle f(x,z,t),\,\Psi_j(x)\Psi_m(z)\right\rangle \\ &\quad\times\left\langle \Psi_k(x)\Psi_m(z),\,g(x,z)\Psi_i(x)\Psi_l(z)\right\rangle, \end{aligned} \tag{8}$$

where summations over indices $j$, $k$ and $m$ represent the $x$ and $z$ coordinates of the wavelet expansions, respectively. An identical compact notation can be used for the partial derivative with respect to the $z$ coordinate. Again, the term $\langle \Psi_j(x), \partial\Psi_k(x)/\partial x\rangle$ is the differential operator in the wavelet basis (Beylkin 1992). The term $\langle f(x,z,t), \Psi_j(x)\Psi_m(z)\rangle$ is the wavelet coefficient of the function $f$ after a 2-D wavelet transform. $\langle \Psi_k(x)\Psi_m(z), g(x,z)\Psi_i(x)\Psi_k(z)\rangle$ can be understood as the function $g$ scaled by using the 2-D wavelet basis. This term represents a huge $(nx\times nz)\times(nx\times nz)$ square matrix. Of course, if the function $g$ turns out to be a constant, the latter term reduces to a scalar $g_0$. *A priori*, this spectral approach is computer-memory intensive compared with the pseudospectral and standard finite-difference approaches. Still, it will be useful for the specific problems we need to treat in the future.

### *SH* velocity–stress formulation in the wavelet domain

Let us consider a 2-D heterogeneous medium characterized by its shear modulus $\mu(x,z)$ and buoyancy $b(x,z)$. The buoyancy is the inverse of the density. The $v_y$ velocity field and $\tau_{xy}$ and $\tau_{zy}$ components verify the first-order hyperbolic system (Virieux 1984) expressed as

$$\begin{cases}\dfrac{\partial v_y(x,z,t)}{\partial t} = b(x,z)\left[\dfrac{\partial \tau_{xy}(x,z,t)}{\partial x}+\dfrac{\partial \tau_{zy}(x,z,t)}{\partial z}\right]+f(x,z,t)\\[2ex] \dfrac{\partial \tau_{xy}(x,z,t)}{\partial t} = \mu(x,z)\,\dfrac{\partial v_y(x,z,t)}{\partial x}\\[2ex] \dfrac{\partial \tau_{zy}(x,z,t)}{\partial t} = \mu(x,z)\,\dfrac{\partial v_y(x,z,t)}{\partial z}\,.\end{cases} \tag{9}$$

The source term $f$ is the surface density of the force applied in the $y$ direction where excitation exists. The first equation of the system is the equation of motion. The other two equations are obtained by differentiation of Hooke's law with respect to time. The temporal differential operator is discretized using centred finite differences. This leads to the following discretized system:

$$\begin{cases} v_y^{n+1/2}(x,z) = v_y^{n-1/2}(x,z)+\Delta t\, b(x,z)\left[\dfrac{\partial \tau_{xy}^n(x,z)}{\partial x}+\dfrac{\partial \tau_{zy}^n(x,z)}{\partial z}\right] \\ \qquad\qquad +\Delta t f^n(x,z,t)\\[2ex] \tau_{xy}^{n+1}(x,z) = \tau_{xy}^n(x,z)+\Delta t\,\mu(x,z)\,\dfrac{\partial v_y^{n+1/2}(x,z)}{\partial x}\\[2ex] \tau_{zy}^{n+1}(x,z) = \tau_{zy}^n(x,z)+\Delta t\,\mu(x,z)\dfrac{\partial v_y^{n+1/2}(x,z)}{\partial z}\,,\end{cases} \tag{10}$$

where the superscript $n$ is the time index and $\Delta t$ the time step for time extrapolation. Each term of eq. (10) is projected on to a 2-D wavelet basis. Each coefficient of the wavelet basis is identified on both left- and right-hand sides of the hyperbolic system. In the wavelet (spectral) domain, this results in the following system,

$$\begin{cases} \langle v_y^{n+1/2}(x,z),\,\Psi_i(x)\Psi_k(z)\rangle \\ \quad = \langle v_y^{n-1/2}(x,z),\,\Psi_i(x)\Psi_k(z)\rangle \\ \qquad +\Delta t\left[\left\langle b(x,z)\,\dfrac{\partial \tau_{xy}^n(x,z)}{\partial x}\,\Psi_i(x)\Psi_k(z)\right\rangle\right. \\ \qquad \left.+\left\langle b(x,z)\dfrac{\partial \tau_{zy}^n(x,z)}{\partial z},\,\Psi_i(x)\Psi_k(z)\right\rangle\right] \\ \qquad +\langle f^n(x,z),\,\Psi_i(x)\Psi_k(z)\rangle \\ \langle \tau_{xy}^{n+1}(x,z),\,\Psi_i(x)\Psi_k(z)\rangle \\ \quad = \langle \tau_{xy}^n(x,z),\,\Psi_i(x)\Psi_k(z)\rangle \\ \qquad +\Delta t\langle \mu(x,z)\dfrac{\partial v_y^{n+1/2}(x,z)}{\partial x},\,\Psi_i(x)\Psi_k(z)\rangle \\ \langle \tau_{zy}^{n+1}(x,z),\,\Psi_i(x)\Psi_k(z)\rangle \\ \quad = \langle \tau_{zy}^n(x,z),\,\Psi_i(x)\Psi_k(z)\rangle \\ \qquad +\Delta t\langle \mu(x,z)\,\dfrac{\partial v_y^{n+1/2}(x,z)}{\partial z},\,\Psi_i(x)\Psi_k(z)\rangle\,. \end{cases} \tag{11}$$

The right-hand side of this system can be estimated using procedures described previously. Time extrapolation is done by simple second-order centred finite differencing. Once coefficients of each field on the left-hand side of the system are obtained, we repeat the operation. If a spatial representation of the wavefield is required for comparison or analysis an inverse wavelet transform at a selected time is performed.

### 2.4 Source excitation in the wavelet domain

We consider a surface density of body forces that is easily implemented by incrementing the velocity wavefield at time $n+1/2$ by the source term $\Delta t f^n(x,z,t)$. This is shown in eq. (10). A surface density of force can be written as

$$f(x,z,t) = \mathscr{S}(t)\mathscr{D}(x-x_s, z-z_s)\,, \tag{12}$$

where the time function $\mathscr{S}(t)$ is the source wavelet, the space function $\mathscr{D}(x,z)$ is the spatial distribution of surface density and $(x_s, z_s)$ are the point source coordinates.

In the wavelet domain the source excitation can be implemented by discretizing $\mathscr{D}(x-x_s, z-z_s)$ in an approximation space $\mathbf{V}_j$. We interpolate the projection $P_{\mathbf{V}_j \times \mathbf{V}_j}\mathscr{D}(x-x_s, z-z_s)$ in $\mathbf{V}_0$ if $j \neq 0$ and compute the 2-D wavelet transform of $P_{\mathbf{V}_0 \times \mathbf{V}_0}\mathscr{D}(x-x_s, z-z_s)$ once. The resulting wavelet coefficients are normalized by the $\mathbf{V}_0$-grid cell surface and multiplied by the time-dependent value of the source time function $\mathscr{S}$ at the current time of propagation. At each time step, each wavelet coefficient of the velocity $v_y$ is incremented by the associated wavelet coefficient of $f$ multiplied by $\Delta t$.

The direct source implementation in the wavelet and space domain provides similar results provided the source extends spatially over several points of the grid $\mathbf{V}_0$. In Fig. 1 the point source function $\mathscr{D}(x, z)$ is discretized in $\mathbf{V}_0$ and smoothed using a 2-D Gaussian function $\mathscr{G}_{\tau_x,\tau_z}(x, z)$. Its correlation lengths ($\tau_x = 60$ m, $\tau_z = 60$ m) were significantly greater than the mesh spacing of $\mathbf{V}_0$ (40 m). Note that the amplitude of the wavelet coefficients of the wavefield decays across scales. This illustrates the regularity of the wavefield.

Dramatic differences are observed between the staggered-grid time–space and the time–wavelet finite-difference simulations when an impulsive point source is discretized on the $\mathbf{V}_0$ grid. For the point source we used a triangular approximation in $x$- and $z$-directions. This corresponds to a 2-D spatial delta function. Fig. 2 shows a snapshot computed using the time–wavelet method using similar model configurations as in Fig. 1, but now exciting the impulsive point source. In Fig. 2(a), high-frequency numerical noise in an ellipsoidal shape is observed. It 'propagates' along the horizontal and vertical axes of the ellipse with a velocity twice as great as the medium velocity. The frequency content of the numerical noise in Fig. 2(a) can be analysed in the wavelet domain (Fig. 2b). This noise is only present at fine scales. For example, the wavefield in $\mathbf{W}_{1_h} \times \mathbf{W}_{1_v}$ is propagating twice as fast as the wavefield in the $\mathbf{V}_{3_h} \times \mathbf{V}_{3_v}$ space. In the $\mathbf{W}_{1_h} \times \mathbf{V}_{3_v}$ space, the wavefield propagation is twice as fast in the vertical compared to the horizontal direction. The wavefield on the coarse approximation subspace $\mathbf{V}_{3_h} \times \mathbf{V}_{3_v}$ is poorly affected by this noise and looks like that of Fig. 1(c) (Fig. 2c).

When Daubechies-8 wavelets are used, the numerical velocity is four times faster than the medium velocity. This noise propagates with a velocity which is dependent on the order of the spatial differential operator associated with the selected wavelet basis.

A further numerical test has been performed by implementing the standard time–space finite-difference method in the $\mathbf{V}_0$ domain using non-staggered grid stencils of coefficients ($-1/12$, $2/3$, $0$, $-2/3$, $1/12$). We remind the reader that these stencils are those used in the time–wavelet algorithm (see Section 2.2). By doing so, we generated the same noise as that shown in Fig. 2(a).

In fact, this noise results from the intrinsic properties of the central finite-difference stencils of the derivative operator. For an impulsive point source, high-frequency waves are excited when standard (i.e. non-staggered) grids are implemented in the finite-difference algorithm. By improving the finite-difference approximation of the spatial operator, regardless of the wavelet basis we use, we may improve the numerical performance of the wavelet approach in the future.

Let us underline the difference between standard and staggered grids by going back to the original development of staggered grids for second-order operators. We consider a time–space

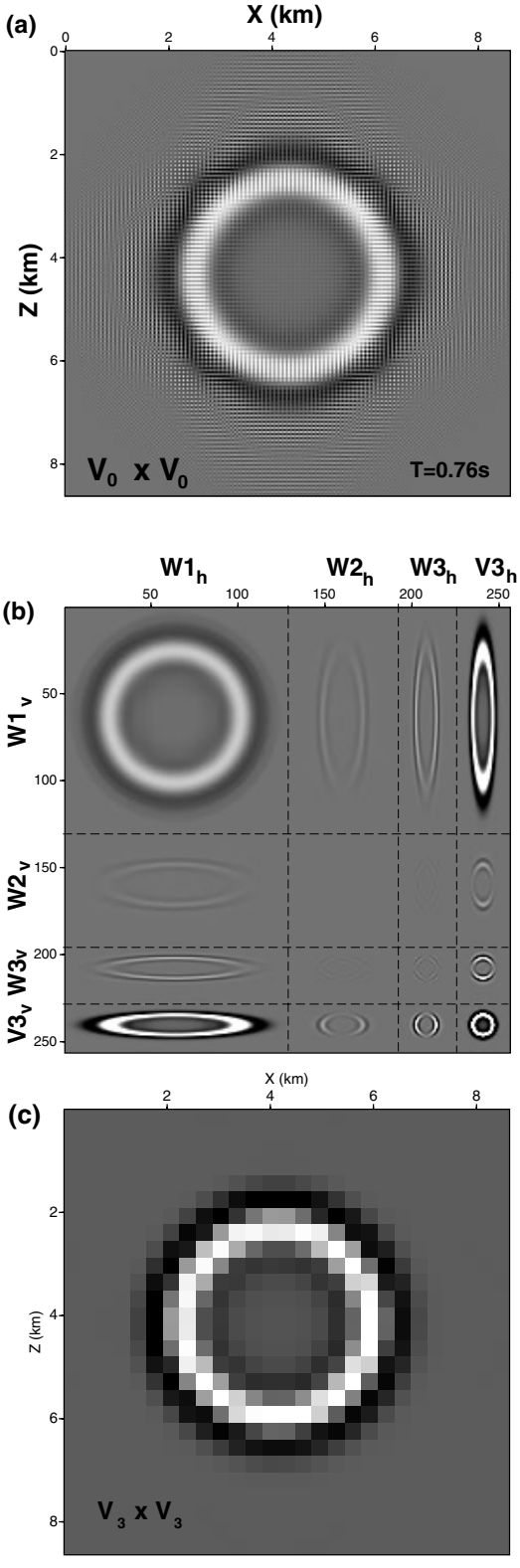


**Figure 2.** (a) Snapshot at $t = 0.76$ s of a 2-D wavefield, emitted by an impulsive point source discretized in $\mathbf{V}_0$ that propagates in a homogeneous medium with velocity 4 km s$^{-1}$ and density 2.5 g cm$^{-3}$. The wavefield is represented in $\mathbf{V}_0$ space of the multiresolution analysis. This figure should be compared with Fig. 1(a). (b) Snapshot as in Fig. 2(a) but now in the wavelet domain. This figure should be compared with Fig. 1(b). (c) Close-up of Fig. 2(b) corresponding to the approximation subspace $\mathbf{V}_{3_h} \times \mathbf{V}_{3_v}$. This figure should be compared with Fig. 1(c).

velocity–stress finite-difference algorithm using central stencils of coefficients (0.5, 0, −0.5) on a standard grid. Excitation of an impulsive point source gives two uncoupled staggered grids: one that is not excited, while the other is related to the source position and will provide the simulation we are interested in. This is the main feature leading to the staggered grid definition that reduces the number of nodes required in a simulation.

We verified such numerical behaviour through a wavelet formulation. A propagation simulation for an impulsive point source was computed using piecewise linear spline bi-orthogonal wavelets (Cohen *et al.* 1992, p. 539). In this case, the finite-difference stencils in the $\mathbf{V}_0$ grid as derived from the wavelet properties have coefficients (−0.5, 0, 0.5). The projection of the differential operator on this bi-orthogonal wavelet basis is equivalent to a second-order finite-difference operator. The grid associated with the velocity is shown in Fig. 3(a). One can guess that every other node is zero. In Fig. 3(c), every other sample in the horizontal and vertical directions was removed. This leads to the desired snapshot (compare Figs 1a and 3c). Staggered grids allow stable finite-difference approximations of the derivative of the impulsive source. In Fig. 3(b), the staggered-grid property is illustrated in the wavelet domain. We observed that a wavefield propagates at the fine scales with the same velocity as that at the coarse scale (compare Figs 1b, 2b and 3b).

Once the efficiency of staggered grids has been established for second-order operators, a direct extension to the fourth-order scheme has been proposed on these staggered grids (Levander 1988). Nevertheless, in the fourth-order case, staggered grids are not directly connected to the usual central finite-difference stencils of coefficients (−1/12, 2/3, 0, −2/3, 1/12). Using the fourth-order scheme results on two staggered grids that are now weakly coupled because of the position of the 1/12 coefficient in the stencil. One should use centred stencils of the form ($a$, 0, $b$, 0, $-b$, 0, $-a$) in order to reproduce uncoupled staggered grids. Implicitly, this has been developed by Levander (1988) in his direct implementation of the fourth-order scheme on to a staggered grid. Another strategy is to force the coupling between the two grids with a technique proposed by Jo *et al.* (1996); Stekl & Pratt (1998). They designed a more complex stencil by combining two rotated grids. This will be analysed in the future.

Another way to force the coupling between grids is the spatial extension of the source that guarantees the excitation of a sufficient number of nodes. The numerical dispersion will still have a behaviour depending on twice the grid step. This spatial spreading has been applied directly on the $\mathbf{V}_0$ grid in Fig. 1. The absence of noise in Fig. 1(a) compared with Fig. 2(a) shows the efficiency of the spatial spreading of the source in coupling the grids. Alternatively, this spread may be obtained by defining the impulsive point source on an intermediate scale of the multiresolution analysis ($\mathbf{V}_j$, $j>0$). This leaves the task of spreading the source on the $\mathbf{V}_0$ grid to the wavelet scaling structure. Of course, the source can be implemented by computing the local analytical solution in a homogeneous region surrounding the source (Alterman & Karal 1968).

### 2.5 PML absorbing boundary condition in the wavelet domain

We use absorbing boundary conditions to compensate the finite model dimensions of our grid. We have implemented the perfectly matched layer condition that was adapted to the

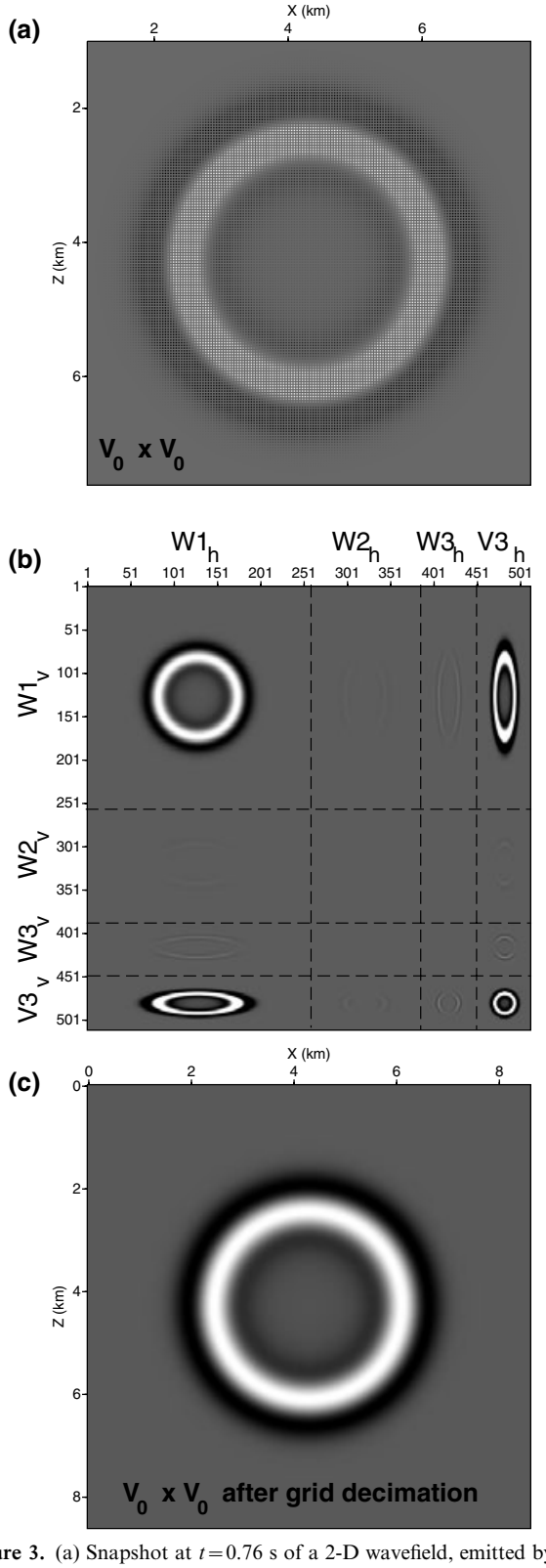


**Figure 3.** (a) Snapshot at $t=0.76$ s of a 2-D wavefield, emitted by an impulsive point source discretized in $\mathbf{V}_0$ that propagates in a homogeneous medium with velocity 4 km s$^{-1}$ and density 2.5 g cm$^{-3}$. Bi-orthogonal linear piecewise linear wavelets were used. The wavefield is represented in $\mathbf{V}_0$ space of the multiresolution analysis. This figure should be compared with Fig. 2(a). (b) Snapshot as in Fig. 3(a) but now in the wavelet domain. This figure should be compared with Fig. 2(b). (c) Same as in Fig. 3(a) after removing every other sample horizontally and vertically.

elastic wave equation by Zhang & Ballmann (1997). Originally, it was developed for electromagnetism (Berenger 1994). The 2-D model is surrounded by absorbing layers characterized by damping factors ($\sigma_x$, $\sigma_z$). These two parameters define a perfectly matched layer. The non-absorbing condition inside the non-absorbing medium is obtained by setting $\sigma$ equal to zero. The absorbing layer along the vertical and horizontal edges are PML media of type ($\sigma_x$, 0) and (0, $\sigma_z$), respectively (see Fig. 2 in Zhang & Ballmann 1997). Our implementation of the PML absorbing boundary condition in the wavelet domain is presented in Appendix C. A comparison between the efficiency of the PML absorbing condition and the sponge-like absorbing boundary condition of Cerjan *et al.* (1985) is illustrated in Fig. 4. We used absorbing layers of thickness equal to approximately four wavelengths for the PML case [this corresponds to 20 grid points in the method of Cerjan *et al.* (1985) and a discretization using five nodes per wavelength].

### 2.6 Free surface implementation in the wavelet domain

The free surface boundary condition has been implemented for both the TPWFD and TWFD method. We set to zero the normal stress component, $\tau_{zy}$ in a zone above the free surface. In the numerical implementation the normal stress component may vanish sharply over one grid step or may decay smoothly over a numerical transition zone.

Standard finite-difference methods directly introduce this transition zone into the modelling grid. Accurately fitting the free surface boundary condition requires the transition zone, in effect the mesh spacing, to be as fine as possible. Since the modelling grid is uniform, the local boundary condition at the free surface may lead to a prohibitively large grid in the TSFD method.

For the wavelet formulation we define the free surface transition at a scale finer than that we consider for our medium discretization. The finest scale should provide a smooth variation of the stress field at the free surface in order to reduce numerical grid dispersion (similar to that observed in Fig. 2). This smooth transition should be seen as a sharp boundary by a coarser scale (which is that selected for considering simulation results) in order to verify the free surface boundary condition.

Computation of the wavefields on fine scales is only necessary in the vicinity of the free surface. This can be achieved in the wavelet domain by forcing to zero the fine-scale wavelet coefficients that lie outside a 'mask' zone centred on the free surface. Moreover, the wavefield on the coarse scale must account for the local contribution from the fine scales in the vicinity of the free surface. This condition is naturally provided by the multiresolution decomposition of the wavelet transform. Compared with standard finite-difference applications we have improved our free surface condition by locally refining the medium discretization.

This boundary condition can be implemented in the wavelet domain following a procedure similar to that for absorbing boundaries. It corresponds to a spatial diagonal operator applied to the normal stress. Its coefficients are unity below the free surface and vanish to zero above the free surface. We project this operator in the wavelet basis and multiply it by the normal stress wavefield at each time step. As for the PML boundary condition, we only keep diagonal coefficients of the wavelet-transformed operator.

## 3 NUMERICAL IMPLEMENTATION OF WAVELET-BASED ALGORITHMS

### 3.1 Two concurrent algorithms

Let us consider computer requirements of the two different numerical strategies for the convolution of medium properties with partial differential operators (TPWFD and TWFD).

Before time extrapolation of wavefields the TPWFD approach requires only computation and storage of differential operators plus the spatial source distribution in the wavelet basis. Of course, during time extrapolation we have to compute forward and inverse wavelet transforms at each time step. This is necessary in order to perform the product of medium properties with spatial wavefield derivatives. This numerical approach requires efficient numerical wavelet transforms, just like the Fourier method for the standard finite-difference method. Dedicated procedures using highly parallel computer structures may enhance the performance of the method to become fast enough to compete with standard finite-difference approaches. We have not yet investigated this possibility.

The TWFD approach requires computation of four matrices of full dimension $(nx \times nz) \times (nx \times nz)$ before time extrapolation of the wavefields. They are stored in sparse format either in core memory or on disk. The matrices result from the convolution of medium properties with the differential operator in the wavelet domain, eq. (8). Even if these matrices need to be computed only once for a given medium, their computation remains very expensive. Moreover, only small models can be considered if all matrices have to be stored in core memory [typically, 2 Gb of RAM are needed for a $256 \times 256$ elastic medium, Operto *et al.* (2000)].

During time extrapolation, computation of one wavelet coefficient of the velocity field requires the computation of a term-to-term product of two $(nx \times nz)$ matrices twice. Similarly, computation of one wavelet coefficient of the stress field requires the computation of one term-to-term product of two $(nx \times nz)$ matrices. These products must be repeated $(nx \times nz)$ times to compute all wavelet coefficients. This number of operations results from the convolution in the wavelet domain of the differential operator with the heterogeneous medium properties, eq. (8).

Although these matrices are sparse the spectral approach turns out to be expensive in terms of memory storage and computational cost. At the present stage of our investigation, this method should not be proposed as an efficient tool for wave propagation simulation, though we stress that it provides a direct control of numerical grid dispersion.

The simulations presented in the Section 4 of this paper have been computed using the TPWFD approach, except for the quarter-plane simulation which involves a homogeneous medium with a free surface. In this special case, each simulation has been computed in the wavelet domain.

### 3.2 Mesh discretization and multiresolution scaling

Standard stability and dispersion analysis based on Fourier approaches seem to be difficult to apply in the wavelet domain. Taking into account the equivalence of the differential operator in the Daubechies4-wavelet basis and the fourth-order finite-difference approximation of the differential operator, we have assumed identical discretization rules to avoid dispersion. We

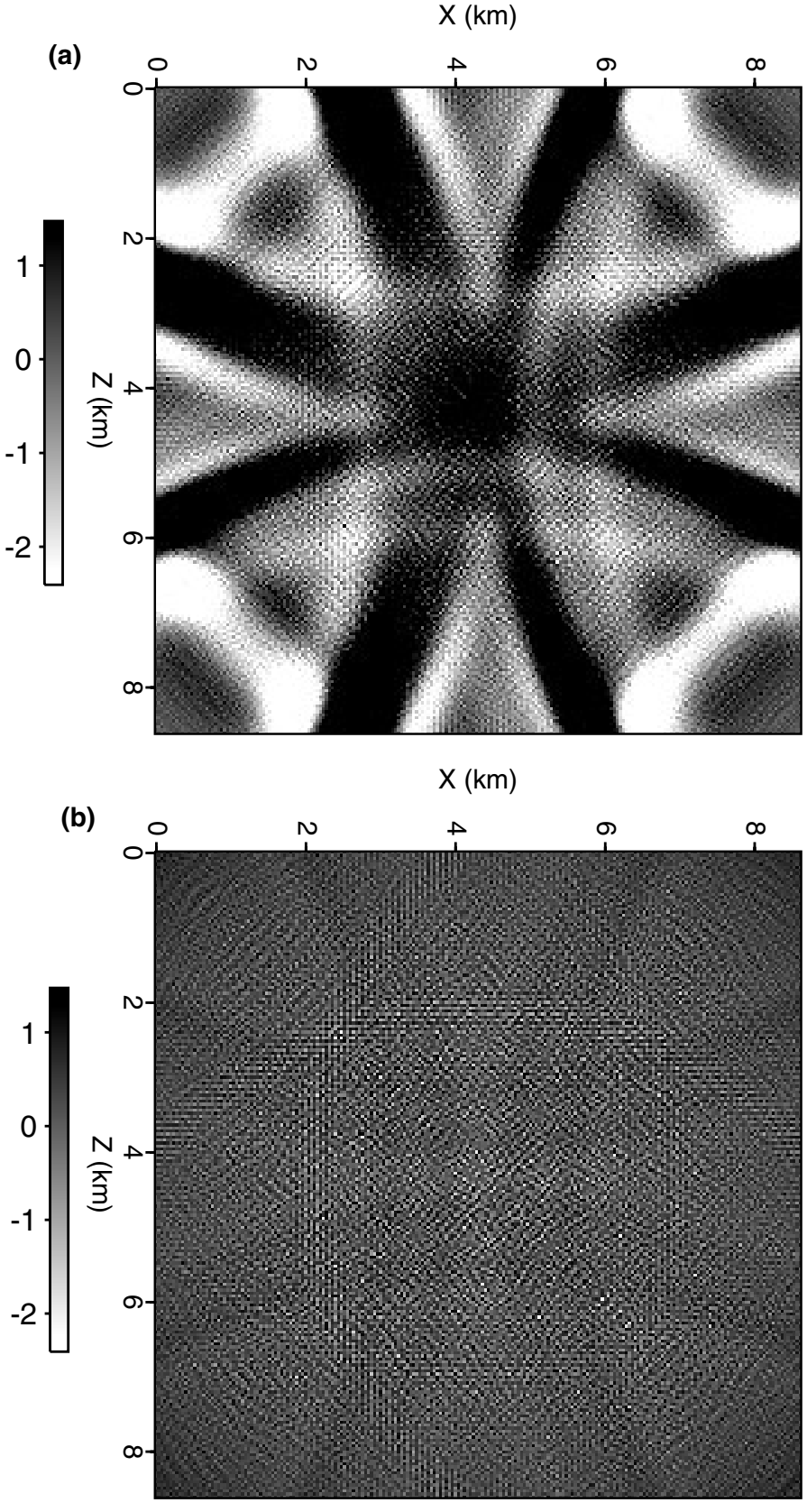


**Figure 4.** Comparison between the PML absorbing boundary condition and the absorbing boundary condition of Cerjan *et al.* (1985) in the wavelet domain. The simulation is the same as that used to create Fig. 1. The dimensions of the model are 8.6 km × 8.6 km and the source is at (4.32 km; 4.32 km). The snapshot was extracted at $t = 2.56$ s in $\mathbf{V}_0$ space. The wavefield has already reached the edges of the model. The two snapshots were multiplied by a factor of 100 and plotted on the same scale as that of Fig. 1. Both simulations were computed using the time–wavelet FD method. (a) Absorbing boundary condition of Cerjan *et al.* (1985). (b) PML absorbing boundary condition.

used five nodes per minimum wavelength for the $\mathcal{O}(\Delta t^2, \Delta x^4)$ time–space scheme as a first guess for the finest discretization of the $\mathbf{V}_0$ space. If the medium exhibits sharp singularities or the wavefield shows strong variations associated with the source excitation, we may increase the number of nodes up to 20 by using the minimum wavelength for the $\mathbf{V}_0$ space.

The choice of the number of scales in the simulation depends on the actual problem at hand. We have selected three to four scales, such that the coarsest scale is discretized with a mesh spacing corresponding to five nodes per maximum wavelength.

The time discretization is common to all scales and is controlled by the finest grid since time adaptivity is not used. Therefore, at the present stage the technique is unattractive in terms of core memory and computation time.

### 3.3 Sparse storage and matrix–matrix product

The TPWFD and TWFD methods require the computation of several sparse matrix–matrix products at each time step. We have used a sparse column storage defined by three vectors: the first vector $v$ contains the elements of the matrix greater than a threshold, the second vector *ic* contains the row index of each non-zero element and the third vector *id* contains the index of the first element greater than the threshold of each column of the matrix in vector $v$. We have implemented the algorithms described in Charton (1996, pp. 51–52).

### 3.4 Space and time adaptivity

The wavefield representation in the wavelet domain may be limited to contain only significant coefficients at several scales without loss of information. Therefore, we do not need to compute all wavelet coefficients at each time step. This procedure is called space adaptivity. Moreover, each scale is associated with a characteristic spatial discretization that should lead to a characteristic time extrapolation discretization as proposed by Bacry *et al.* (1992).

We have found the coupling between scales to be quite cumbersome for the implementation of time adaptivity. Until now we have been unable to design a suitable wavelet decomposition where coupling becomes negligible.

We have implemented two numerical strategies to perform space adaptivity: one based on a threshold criteria and one based on *a priori* constraints.

### 3.5 Thresholding

Space adaptivity can be implemented by thresholding in the wavelet domain. The wavefield is compressed by thresholding before the differential operator is applied to it. This implies that all wavelet coefficients lower than the threshold will not be processed. The threshold can be defined as a percentage of the maximum amplitude of the wavelet coefficients. Note that the threshold may be scale-dependent. For example, if a decay of wavelet coefficients is assumed at fine scales, one may use a higher threshold at fine compared with coarser scales.

### 3.6 Application of masks

Since sharp thresholding leads to significant numerical pollution we also tested *a priori* constraints. These constraints consist of designing masks in the wavelet domain with values of 0 or 1. Wavelet coefficients with associated values of 0 in the mask will never be propagated. We used mainly two pragmatic criteria to design these masks. One is related to the wavelength. In smooth parts of the medium wavelet coefficients are propagated only if the mesh spacing in the associated scale is greater than $N\lambda$, where $\lambda = c f_{\max}$, with $c$ being the local velocity at the wavelet coefficient position, $f_{\max}$ the maximum frequency of the source bandwidth and $N$ the number of points per wavelength. Typically, we used $N = 10$ to guarantee accurate results. The second criterion concerns the presence of discontinuities in the model. They can be examined by analysis of the amplitude of the medium wavelet coefficients after a wavelet transform. We designed masks such that the wavelet coefficients located in the zones of the model exhibiting discontinuities are propagated at each scale of the multiresolution analysis.

Using these two techniques we have increased the efficiency of the wavelet approach. Still the comparison with standard finite-different schemes did not give superior results.

## 4 NUMERICAL SIMULATIONS

### 4.1 Benchmark test: the quarter-plane problem

To verify the accuracy of both our time–space and time–wavelet FD algorithms, we first compare the solutions to these algorithms with an analytical solution for the quarter-plane problem (Virieux 1984). We consider a homogeneous medium of velocity 4 km $s^{-1}$ and density 2.5 g $cm^{-3}$. Since the medium is homogeneous all simulations were computed in the wavelet domain. The dimensions of the model are 4 km $\times$ 4 km. The impulsive point source is located at (2, 1) km. The source wavelet is a Gaussian given by $\mathcal{S}(t) = (t - t_0)\, e^{-\alpha(t-t_0)^2}$ with $t_0 = 0.35$ s and $\alpha = 100$. The maximum frequency is around 13 Hz. In the TWFD method, the delta function source distribution was discretized in the subspace $\mathbf{V}_1$ and oversampled in $\mathbf{V}_0$ to avoid numerical pollution as shown in Fig. 2. The boundary conditions along the edges of the model are free surface conditions for the left-hand and upper edges, and PML absorbing conditions for the right-hand and bottom edges. The analytic solution was computed using image theory as described in Virieux (1984). For the TSFD method, we used a mesh spacing of 40 m and a time step of 0.002 s. For the TWFD method, we first considered a mesh spacing of 5 m in $\mathbf{V}_0$ and three levels in the multiresolution analysis (this implies the discretization of the coarsest subspace $\mathbf{V}_3$ with a 40 m mesh spacing). The time step for time extrapolation is $0.25 \times 10^{-3}$ s. For the TSFD method, the free surface is implemented as a sharp boundary that corresponds to the 40 m mesh spacing of the TSFD grid. For the TWFD method, the free surface is implemented as a sharp boundary for a 20 m grid step, which corresponds to four mesh spacings in the $\mathbf{V}_0$ grid. We have chosen a grid which is twice as fine as that used for the TSFD method because the TWFD does not use staggered grids (see Section 2.2). For the TWFD formulation, we deduce the discretization of the medium on the grid of $\mathbf{V}_0$ by linearly oversampling the medium discretized on to the $\mathbf{V}_2$ grid.

Two snapshots at $t = 0.9$ s (Figs 5a and c) and $t = 1.25$ s (Figs 5b and d) were computed using the TWFD method. They are presented after recomposition in the $\mathbf{V}_0 \times \mathbf{V}_0$ space in Fig. 5(a) and (b). The direct wave, the reflections from the two free boundaries and the reflection from the corner can be

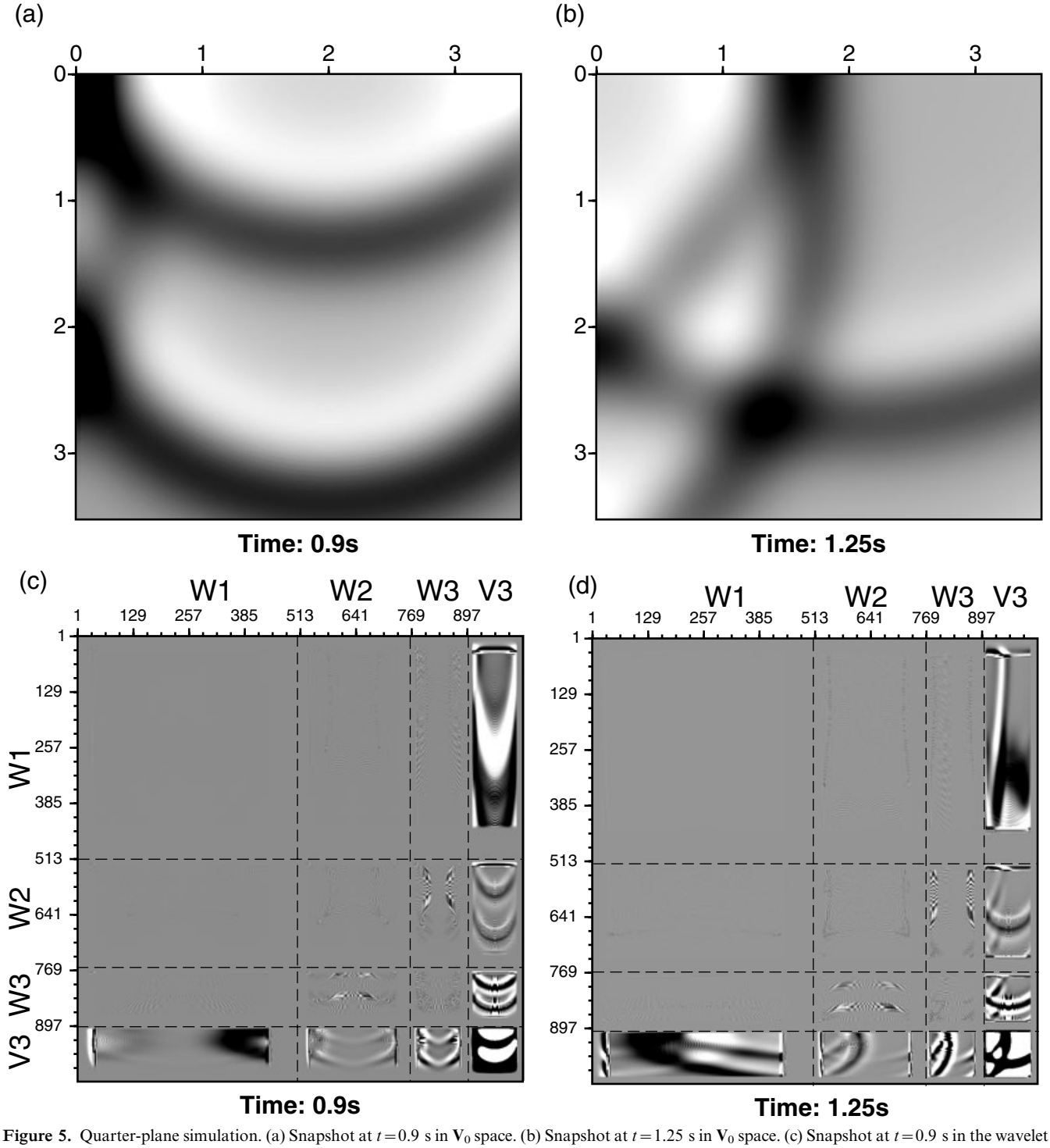


**Figure 5.** Quarter-plane simulation. (a) Snapshot at $t = 0.9$ s in $\mathbf{V}_0$ space. (b) Snapshot at $t = 1.25$ s in $\mathbf{V}_0$ space. (c) Snapshot at $t = 0.9$ s in the wavelet domain. (d) Snapshot at $t = 1.25$ s in the wavelet domain.

observed in both figures. The same snapshots are presented in the wavelet domain in Figs 5(c) and (d). Note the overall decay of the wavelet coefficients across the scales, except for the wavelet coefficients located in the vicinity of the free surface. This illustrates the automatic detection of singularities in the wavefields at the free surface using the wavelet transform. Seismograms computed using the analytical solution and the TWFD method for receivers located at 2 km depth are compared in Fig. 6. The overall agreement is excellent. A more detailed analysis (Fig. 7a) shows the direct comparison of several seismograms computed using the analytical, the TSFD and the TWFD methods. The agreement between the analytical and the TSFD methods is excellent. The seismograms computed using the TWFD method compare well for the direct wave. The reflections exhibit a slight time delay and amplitude loss, in particular the reflection from the corner. These inaccuracies are related to the mesh spacing in $\mathbf{V}_0$. In Fig. 7(b) seismograms are computed using a 20 m mesh spacing instead of 5 m in $\mathbf{V}_0$ for

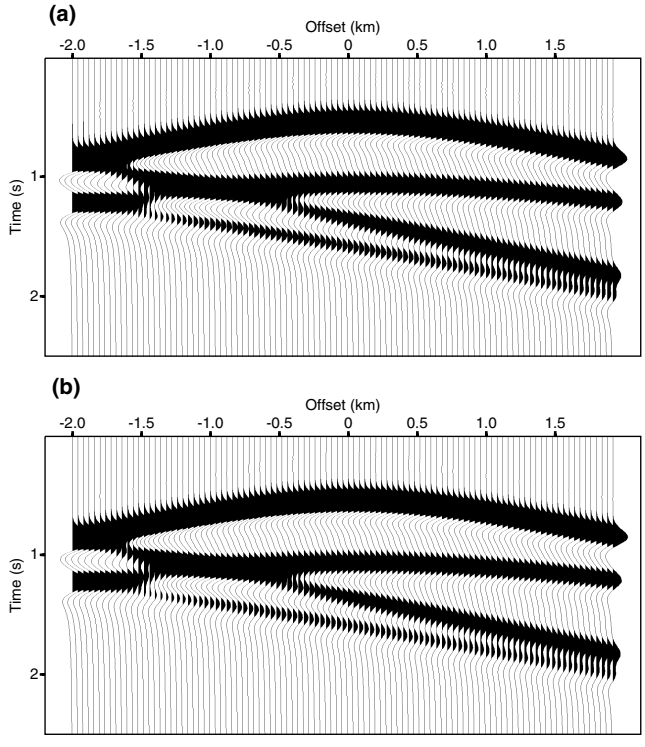


**Figure 6.** Quarter-plane simulation. (a) Seismograms obtained with the analytical solution. (b) Seismograms obtained with the TWFD method. The receivers are located along a horizontal line at 2 km depth.

the example of Fig. 7(a). Note how the time delay and amplitude loss of the reflections in the TWFD seismograms increase as grids become coarser. The TPWFD and TWFD methods are less accurate than the TSFD method when wave reflections from sharp boundaries are treated provided a similar grid selection is used. The use of a non-staggered grid and the choice of the Daubechies non-symmetric basis may induce this degraded performance in the wavelet approach. Note that we may choose grid steps for comparably accurate signals at the expense of computer requirements. Inaccuracies of the TPWFD/TWFD methods arise only in case of contrasted models. The investigation into an optimal wavelet basis is not discussed here.

Replacing a sharp free surface over 40 m thickness by a smooth free surface over 200 m thickness in the two TWFD and TSFD models results in an excellent agreement between the two numerical approaches (Fig. 7c). Though an expected time delay and amplitude loss are observed with respect to the analytical solution.

### 4.2 The corner–edge model

The corner–edge model consists of two homogeneous half-spaces delineated by horizontal and vertical interfaces making a corner. The velocities in the two half-spaces were chosen to be 2 and 8 km $s^{-1}$, respectively, in order to generate a sharp reflection at the interface. The density is 2000 and 2500 kg $m^{-3}$, respectively. The dimensions of the model are 18 km $\times$ 18 km. The four edges of the model are treated using PML absorbing boundary conditions.

The source is distributed using a smoothed point source located at (3.5 km, 8 km). The impulsive point source discretized in $\mathbf{V}_0$ is smoothed with a 2-D Gaussian function with a correlation length of 60 m in both directions. As a source wavelet we applied a Gaussian derivative $\mathscr{S}(t) = -2\alpha(t-t_0)\, e^{-\alpha(t-t_0)^2}$ with $\alpha = 100$ and $t_0 = 0.35$ s. This leads to a source with a central frequency at 2.5 Hz and a maximum frequency of 13 Hz.

For the TSFD method, the model is discretized with a mesh spacing of 40 m. This fits the five nodes per wavelength condition for a velocity of *2* km $s^{-1}$.

For the TPWFD, we present a simulation with 20 m mesh spacing for $\mathbf{V}_0$ and three levels in the multiresolution analysis (this gives a mesh spacing of 160 m in the $\mathbf{V}_3 \times \mathbf{V}_3$ grid that fits the five nodes per wavelength condition for a velocity of

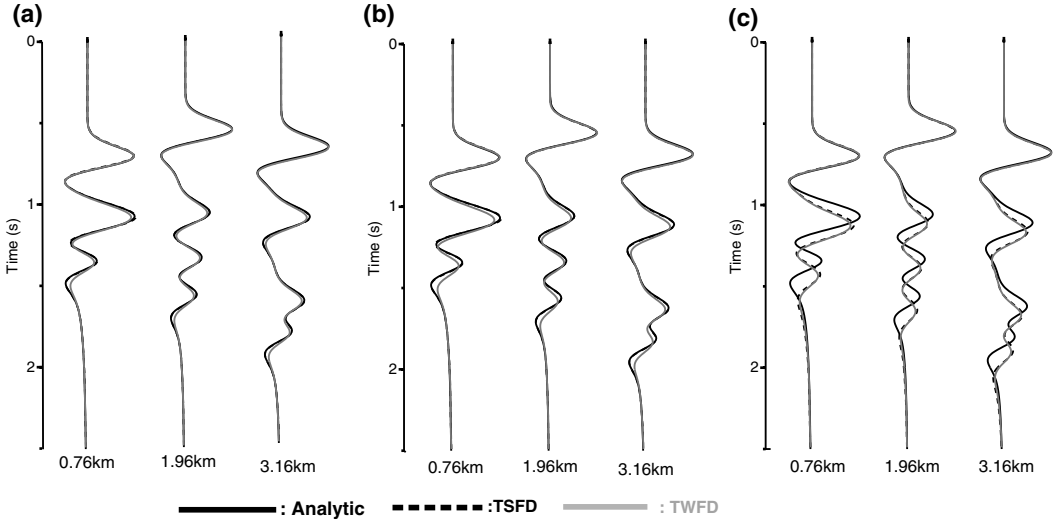


**Figure 7.** Quarter-plane simulation. Direct comparison of seismograms computed using the analytical solution, the TSFD and the TWFD method. (a) The mesh spacing in $\mathbf{V}_0$ is 5 m for the TPWFD method. (b) The mesh spacing in $\mathbf{V}_0$ is 20 m for the TPWFD method. (c) The free surface used in the FD methods is a 200 m thick smooth transition zone. In this case, the TWFD seismograms fit the TSFD seismograms very well.

8 km $s^{-1}$). The dimension of the $\mathbf{V}_0$ grid is $1024 \times 1024$. The model was originally discretized in the $\mathbf{V}_1$ grid and linearly interpolated in the $\mathbf{V}_0$ grid for the simulation. This implies that the discrete representation of the interfaces for both the TSFD and TPWFD methods corresponds to a 40 m thick transition zone.

In Fig. 8(a) we present a snapshot in $\mathbf{V}_0 \times \mathbf{V}_0$ that was computed using the TPWFD method. The arrow points to high-wavenumber noise that is generated when the incident wave reflects from the horizontal interface. It propagates twice as fast as the reflection from the interface. This noise has the same origin as that identified for the impulsive point source simulation (Fig. 2), except that it is generated by the (fine) horizontal scale only. This can be checked by examining the snapshot in the wavelet domain (Fig. 8b). The arrow in the $(\mathbf{V}_{3_h} \times \mathbf{W}_{1_v})$ marks the high-amplitude high-wavenumber signal that was previously identified in the $\mathbf{V}_0 \times \mathbf{V}_0$ space. The wavelength of the signal is twice as large as the wavelength of the reflection from the horizontal interface since it propagates twice as fast. This coherent noise is almost only present in the subspace combining the finest vertical and coarsest horizontal scale of the multiresolution analysis. When reconstructing the snapshot in the $(\mathbf{V}_{0_h} \times \mathbf{V}_{0_v})$ space, the signal contains only high-wavenumber components. Fig. 9 shows a close-up of Fig. 8(b) centred on the approximation space $(\mathbf{V}_{3_h} \times \mathbf{V}_{3_v})$. The artefact has a negligible effect on this coarse representation of the signal owing to the weak coupling between the finest and the coarsest scales. Seismograms recorded by a horizontal line of receivers, spaced 160 m at depth of 2000 m, are shown in Figs 10(a) and (b) for TSFD and TPWFD methods, respectively. A visual comparison between the two sets of seismograms shows good agreement. The main difference is the noise reflection in Fig. 10(b). This reflection does not seem to be of high frequency because we stored the TPWFD seismograms with a sampling rate of $8 \times 10^{-3}$ s while the time step for time extrapolation was $0.5 \times 10^{-3}$ s. Fig. 10(c) shows the seismograms computed using the TPWFD method but now extracted from the coarse approximation space $(\mathbf{V}_{3_h} \times \mathbf{V}_{3_v})$. In this case, the artificial reflection has a very weak amplitude and the seismograms of Figs 10(a) and (c) compare quite well.

A more detailed comparison of the accuracy was performed by making a direct comparison between selected seismograms (Fig. 11). Apart from the noise mentioned previously,

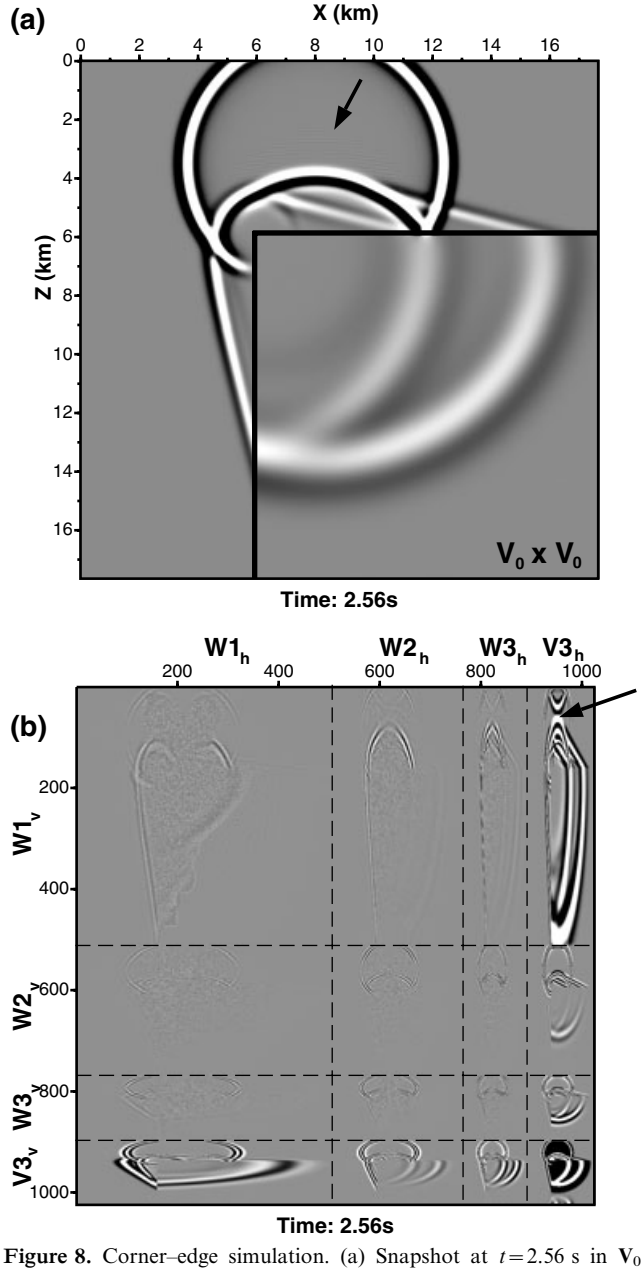


**Figure 8.** Corner–edge simulation. (a) Snapshot at $t = 2.56$ s in $\mathbf{V}_0$ space. (b) Snapshot at $t = 2.56$ s in the wavelet domain. The arrows point to numerical pollution resulting from reflections on the horizontal interface. The pollution propagates in the fine-scale subdomain $\mathbf{W}_{1_v} \times \mathbf{V}_{3_h}$ with a velocity of 4 km $s^{-1}$. Owing to the coupling between scales, this noise can also be identified in the $\mathbf{W}_{3_v} \times \mathbf{V}_{3_h}$ and $\mathbf{V}_{3_v} \times \mathbf{V}_{3_h}$, though the amplitude is much weaker.

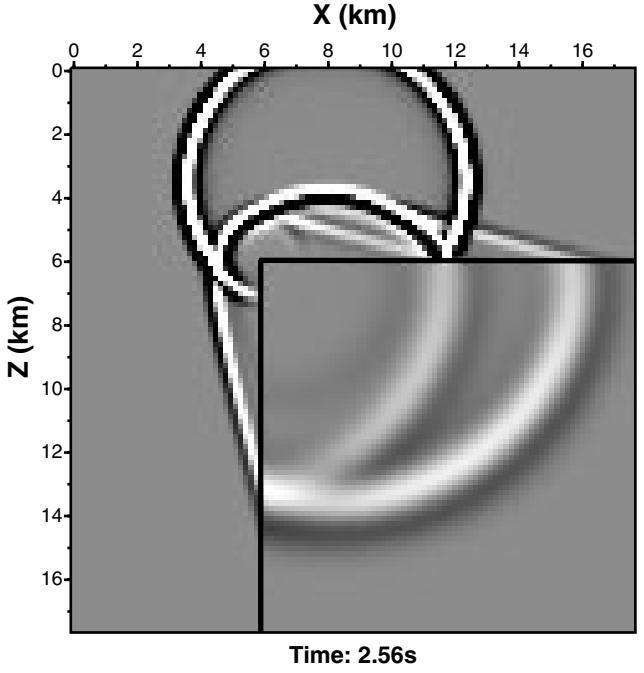


**Figure 9.** Corner–edge simulation. Close-up of Fig. 8(b) centred on the approximation space $\mathbf{V}_3$. Note that the noise identified in Fig. 8(a) is negligible in this approximation space.

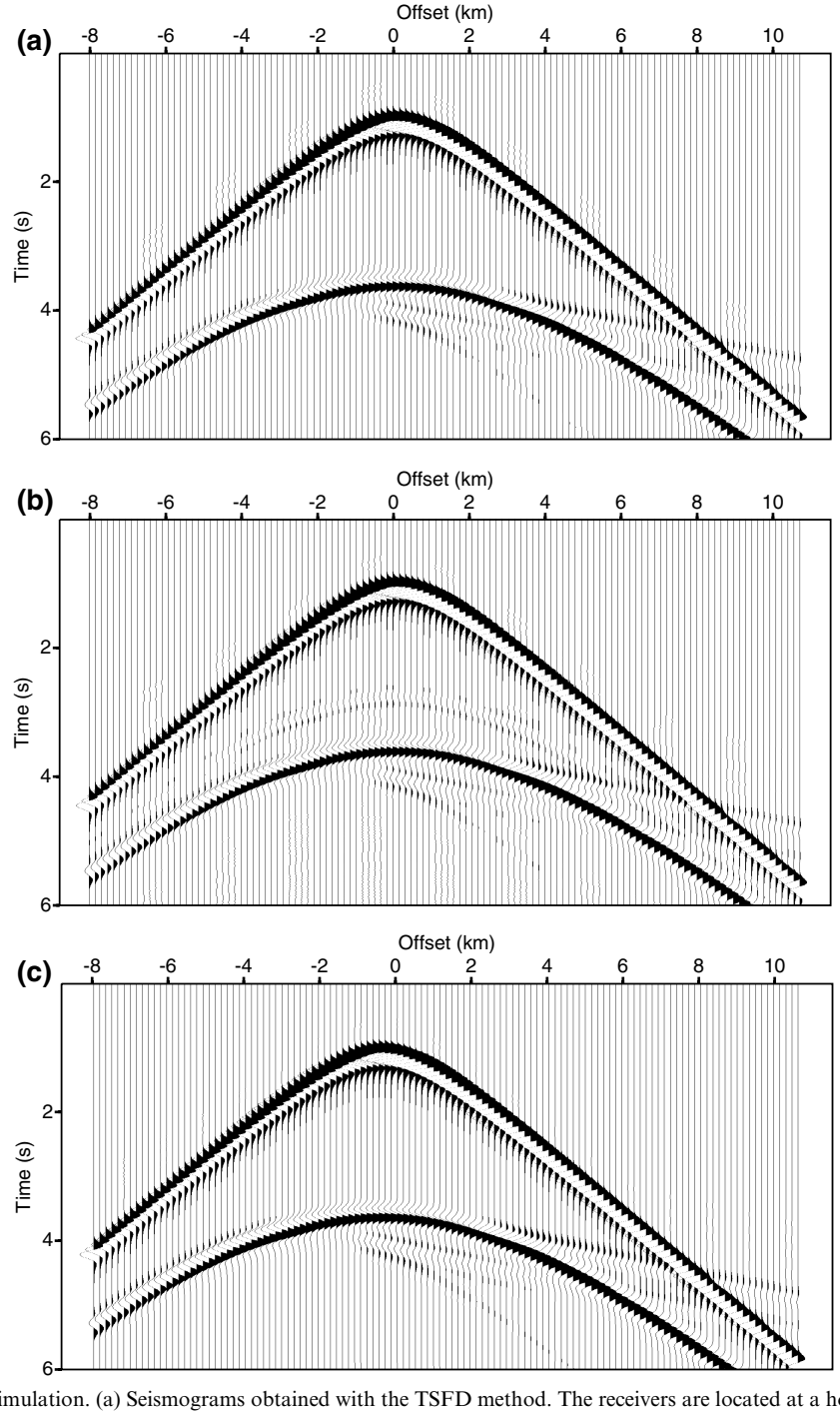


**Figure 10.** Corner–edge simulation. (a) Seismograms obtained with the TSFD method. The receivers are located at a horizontal line at 2 km depth. (b) Seismograms extracted in the $\mathbf{V}_0$ space, computed using the TPWFD method.

the agreement is good. Though we note some slight delay in the seismograms computed using TPWFD. Note that the high-wavenumber noise would probably be removed by adding a finer scale to the multiresolution analysis. We have already observed decreasing noise amplitude compared with a preliminary simulation (not shown here) where we used a grid discretized of 40 m in $\mathbf{V}_0$.

The simulation for the $1024 \times 1024$ $\mathbf{V}_0$ grid with 12 000 time steps required 25, 29 h of CPU on a 600 MHz Linux PC with and without applying the masks described in the paragraph '*Space adaptivity*', respectively (Fig. 12). Again, we remind the reader that the CPU cost is essentially related to the efficiency of the discrete wavelet transform and the sparse matrix–matrix product algorithms that are called at each time step of the time extrapolation.

### 4.3 The structurally complex Marmousi model

We present simulations performed in a windowed part of the Marmousi model (Bourgeois *et al.* 1991). Compared with the

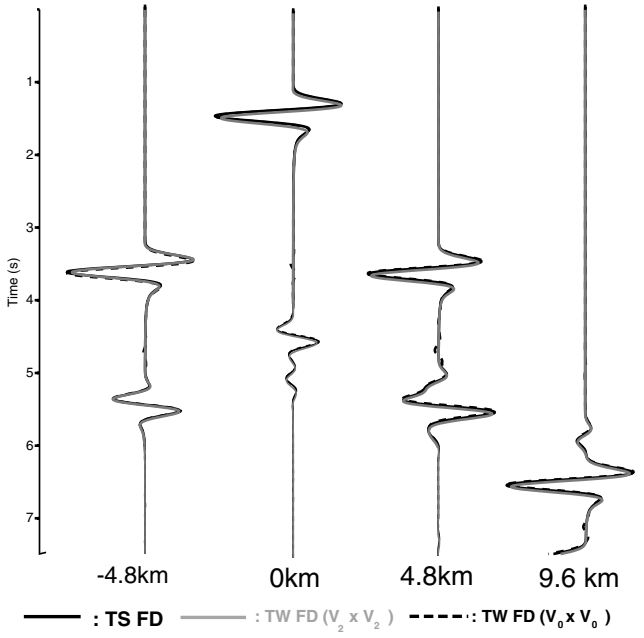


**Figure 11.** Corner–edge simulation. Direct comparison between seismograms computed using the TSFD and the TPWFD method.

corner–edge model, this case study is used to test the accuracy of the TPWFD method against a model exhibiting complex geometry.

The point source is spatially smoothed with a 2-D Gaussian function of 100 m correlation length in each dimension. The source wavelet is a Gaussian derivative with a central, maximum frequency at 10 and 50 Hz, respectively. The source is located in the water layer at (3, 0.7) km.

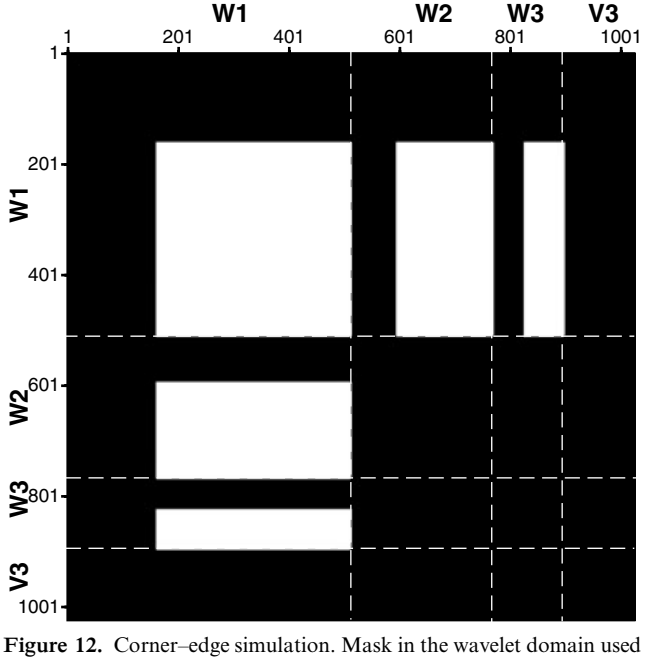


**Figure 12.** Corner–edge simulation. Mask in the wavelet domain used to limit the number of wavelet coefficients propagated during the simulation. Only wavelet coefficients located in the black area will be propagated. Use of this mask allows a 16 per cent CPU time saving.

The 4.092 km × 4.092 km model is discretized using a mesh spacing of 4 m for the TSFD method. This gives a grid of $1024 \times 1024$ nodes. The time step for time extrapolation is $1.5 \times 10^{-4}$ s. A 4 m mesh spacing of $\mathbf{V}_0$ and two decomposition levels were applied for the TPWFD method. This implies a 16 m mesh spacing for the coarsest approximation subspace

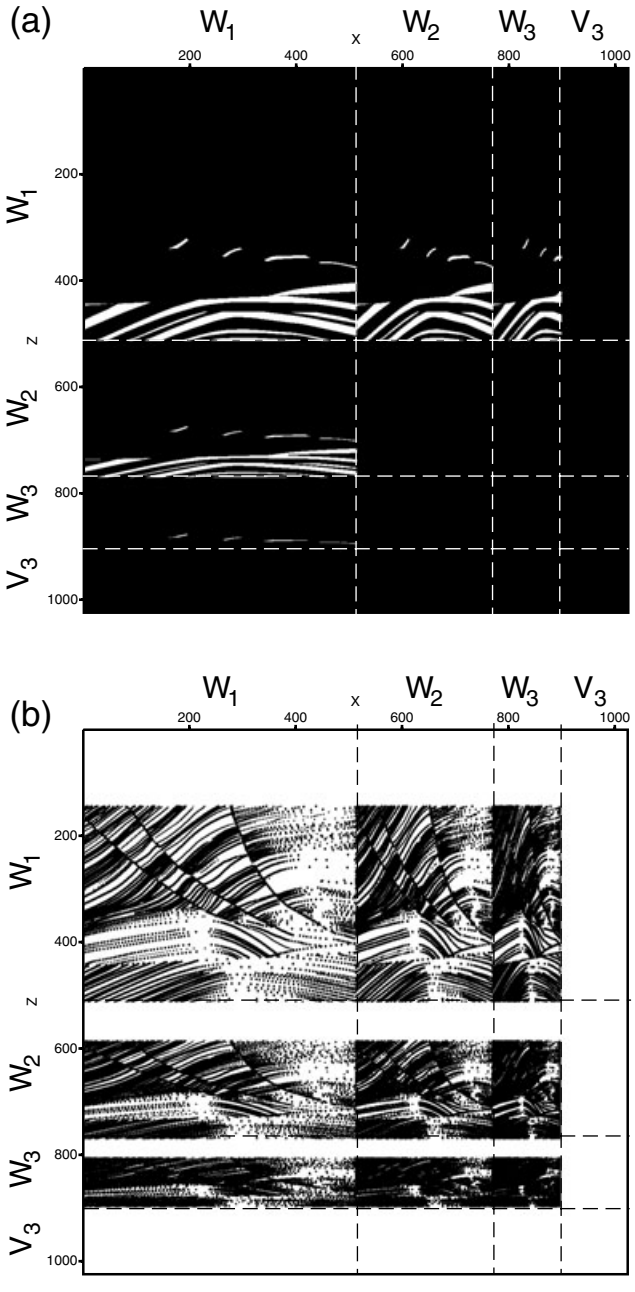


**Figure 13.** Marmousi simulation. Masks used to limit the number of computed coefficients. (a) Mask resulting from the wavelength *a priori* constraint. The wavelet coefficients located in the white areas belong to grids with more than 10 nodes per local wavelength. (b) Mask resulting from the discontinuity *a priori* constraint. The black areas represent portions of the model where the 2-D wavelet transform of the medium detected discontinuities. The area where the wavelet coefficients will be computed is obtained by the union of the black areas of Figs 13(a) and (b). Note that in the case of the Marmousi model the benefit provided by the mask is negligible because the velocity field is not contrasted enough to have a significant effect.

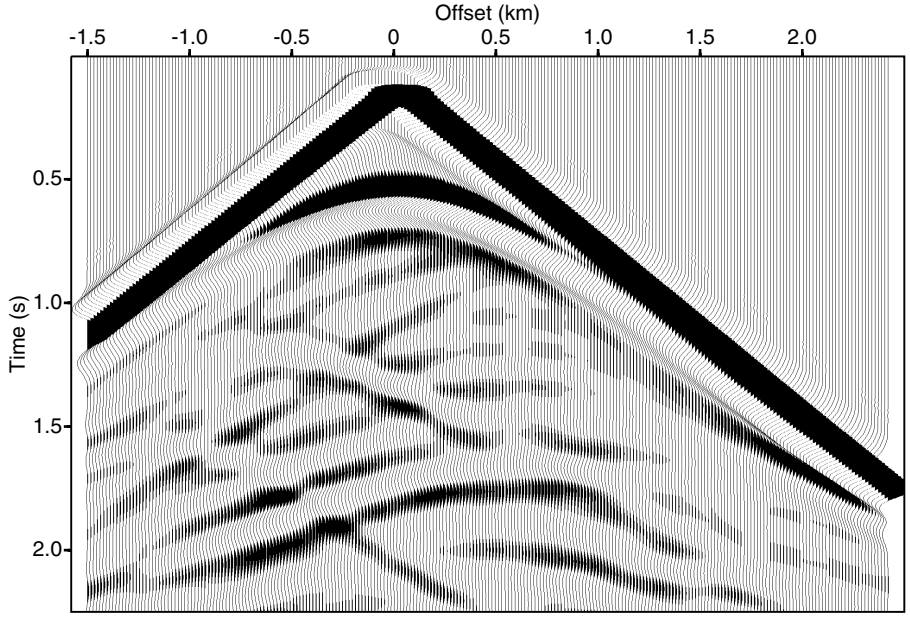


**Figure 14.** Marmousi simulation. Seismograms computed using the TPWFD method.

$\mathbf{V}_2$ which approximately fits the five nodes per maximum wavelength condition. The masks used to limit the number of computed wavelet coefficients are shown in Fig. 13.

In Fig. 14, we plot TPWFD seismograms recorded by a receiver line at 0.7 km depth. The direct comparison of several seismograms computed using the TPWFD and TSFD methods (Fig. 15) shows excellent agreement throughout.

This case study confirms the conclusions of the two previous examples. TSFD and TPWFD methods are in excellent agreement provided the wavefield and medium are regular (i.e. when their derivatives are continuous although they may vary rapidly as for the Marmousi model). In this case, the $\mathbf{V}_0 \times \mathbf{V}_0$ approximation space can be discretized using the same mesh spacing as for the TSFD method. The number of levels in the multiresolution analysis will be defined with respect to the largest wavelength to be modelled.

In contrast, if the wavefield exhibits a singular behaviour at the source or at sharp interfaces, the TPWFD method requires very fine mesh spacing because staggered grids are not used. This is demonstrated by high-frequency numerical noise in the solution. It results from the propagation of high-amplitude fine-scale wavelet coefficients. A pragmatic way to remove this noise is the discretization of the $\mathbf{V}_0$ space such that step functions are interpolated on two scales. Similar rules apply

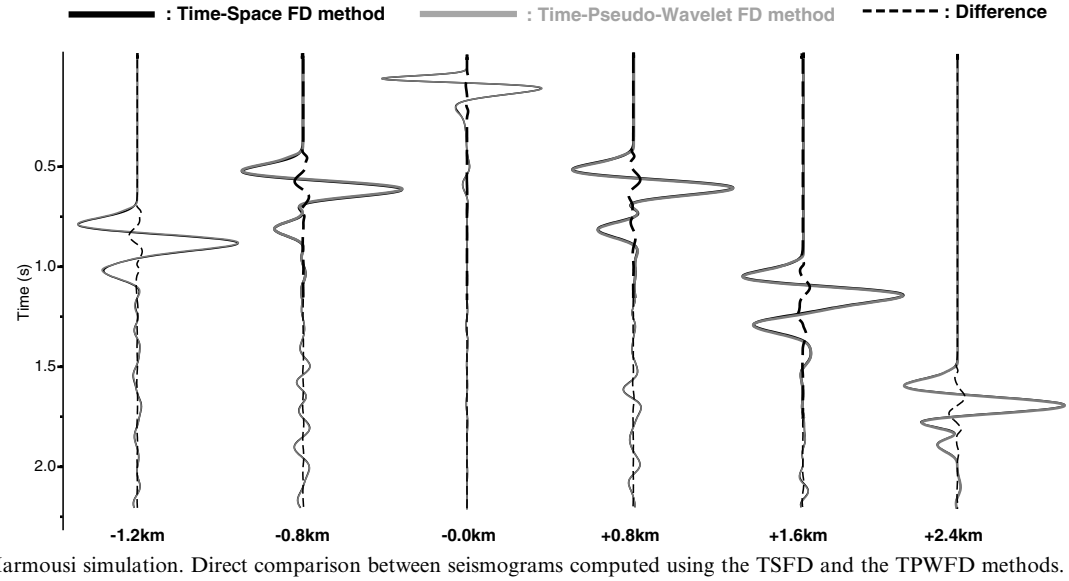


**Figure 15.** Marmousi simulation. Direct comparison between seismograms computed using the TSFD and the TPWFD methods. The dotted line represents the difference between the logs obtained with the TSFD and TPWFD methods.

for the source distribution. Interpretative results will be considered on a coarser grid associated with a space $\mathbf{V}_j$ which are not polluted by the high-frequency noise. In other words, the physical description of the source of the medium will be the same for both TSFD and TPWFD/TWFD methods. However, the discretization will be finer in the latter two cases.

## 5 CONCLUSION

We have presented an adaptive finite-difference method for *SH*-wave propagation modelling based on the discrete wavelet transform and multiresolution analysis. We proposed two possible formulations of the method. The TWFD approach performs simulations completely in the wavelet domain. The TPWFD method requires the forward and back transformation of the wavefield into the space domain in order to perform efficiently the multiplication of the spatial wavefield derivative with the medium properties.

The first approach turns out to be very expensive in terms of memory and computational cost if no additional approximation is used. Nevertheless, if the medium is assumed to be locally homogeneous, this approach may be competitive with other finite-difference methods (Wu & McMechan 1998). Since we are interested in modelling waves in contrasted heterogeneous media, this first approach was not investigated any further here.

At the present stage of our work, the second formulation is not yet competitive with standard time–space finite-difference methods, though space adaptivity was implemented. The performance of the method is closely related to the efficiency of the discrete wavelet transform algorithm. We used standard algorithms that do not exploit the potential sparsity of the wavefield in the wavelet domain. Using highly optimized routines might considerably reduce computational costs in the future. The computational efficiency is further limited by the fact that we have not yet been able to implement time adaptivity. Its implementation will be our next investigation (Bacry *et al.* 1992).

The selection of an optimal wavelet basis for the wave modelling problem is another crucial point. We have selected the Daubechies wavelet basis for their local support and the close relationship between the projection of the differential operator in this basis and its finite-difference approximation. Wavelet bases having better regularity properties may optimize the compression of the wavefield. Furthermore they may avoid numerical pollutions at fine scales when singular wavefields are involved in the modelling.

Despite of the present limitations, our simulations in very contrasted (corner–edge) or structurally complex (Marmousi) models show that the wavelet approach is worth investigating.

Yet, the time–wavelet finite-difference method cannot be considered as a practical tool for wave propagation modelling in terms of CPU efficiency. Still it provides an invaluable tool for analysing the contribution of different scales during wave propagation. For example, it allows one to model a wave phenomenon at a given coarse resolution while accounting for the contribution coming from finer scales. We believe that the fine-scale contributions have a significant influence on the exact solution in the case of specific problems such as non-linear rheology of unconsolidated materials or crack propagation modelling.

## ACKNOWLEDGMENTS

We thank K. Wapenaar and an anonymous referee for their comments. The research leading to this paper was partly founded by DASE/CEA through the PROSIS3D group. The authors thank S. Gaffet (UMR Geosciences Azur, CNRS, France) for some fruitful discussions. This paper is Contribution No. 418 from UMR Geosciences Azur, CNRS, France.

## REFERENCES

Alterman, Z. & Karal, F.C., 1968. Propagation of elastic waves in layered media by finite difference methods, *Bull. seism. Soc. Am.,* **58,** 367–398.

Aoi, S. & Fujiwara, H., 1999. 3D finite-difference method using discontinuous grids, *Bull. seism. Soc. Am.,* **89,** 918–930.

Bacry, E., Mallat, S. & Papanicolaou, G., 1992. A wavelet based space-time adaptive numerical method for partial differential equations, *Math. Model. Numer. Anal.,* **26,** 793–834.

Berenger, J.P., 1994. A perfectly matched layer for the absorption of electromagnetic waves, *J. Comp. Phys.,* **114,** 185–200.

Berger, M.J. & LeVeque, R., 1998. Adaptive mesh refinement using wave propagation algorithms for hyperbolic systems, *SIAM J. Numer. Anal.,* **35,** 2298–2316.

Berger, M.J. & Oliger, J., 1984. Adaptive mesh refinement for hyperbolic partial differential equations, *J. Comp. Phys.,* **53,** 484–512.

Beylkin, G., 1992. On the representation of operators in bases of compactly supported wavelets, *SIAM J. Numer. Anal.,* **6,** 1716–1740.

Biswas, R., Flaherty, J.E. & Arney, D.C., 1993. An adaptive mesh-moving and refinement procedure for one-dimensional conservation laws, *Appl. Numer. Math.,* **11,** 259–282.

Boore, D.M., 1972. Finite-difference methods for seismic wave propagation in heterogeneous materials, in *Methods in Computational Physics,* Vol. 11, ed. B.B.A., Academic Press, New York.

Bourgeois, A., Bourget, M., Lailly, P., Poulet, M., Ricarte, P. & Versteeg, R., 1991. Marmousi, model and data. In *The Marmousi Experience,* pp. 5–16. Eur. Ass. Expl. Geophys.

Cerjan, C., Kosloff, D., Kosloff, R. & Reshef, M., 1985. A nonreflecting boundary condition for discrete acoustic and elastic wave equations, *Geophysics,* **50,** 2117–2131.

Charton, P., 1996. Produits de matrices rapides en bases d'ondelettes: application à la résolution numérique d'équations aux dérivés partielles, *PhD thesis,* University of Paris Nord.

Cohen, A., Daubechies, I. & Feauveau, J.-C., 1992. Biorthogonal bases of compactly supported wavelets, *Comm. Pure Appl. Math.,* **45,** 485–560.

Daubechies, I., 1988. Orthonormal bases of compactly supported wavelets, *Comm. Pure Appl. Math.,* **41,** 909–996.

Daubechies, I., 1992. *Ten Lectures on Wavelets,* SIAM CBMS61.

Day, S., 1982. Three-dimensional simulation of spontaneous rupture: the effect of non-uniform prestress, *Bull. seism. Soc. Am.,* **72,** 1881–1902.

Dormy, E. & Tarantola, A., 1995. Numerical simulation of elastic wave propagation using a finite volume method, *J. geophys. Res.,* **100,** 2123–2133.

Graves, R.W., 1996. Simulating seismic wave propagation in 3D elastic media using staggered-grid finite differences, *Bull. seism. Soc. Am.,* **86,** 1091–1106.

Hestholm, S., 1999. 3-D finite-difference visocelastic wave modeling including surface topography, *J. Sci. Comp.,* **139,** 852–878.

Jameson, L., 1993. On the wavelet based differentiation matrix, *J. Sci. Comp.,* **8,** 267–305.

Jo, C.H., Shin, C.S. & Suh, J.H., 1996. An optimal 9 point, finite difference, frequency-space, 2-D wave extrapolator, *Geophysics,* **61,** 529–537.

Joly, P., Komatitsch, D. & Vilotte, J., 1995. The solution of the wave equation by wavelet basis approximation, *Proc. Enumath'95 Conf.*

Joly, P., Maday, Y. & Perrier, V., 1994. Towards a method for solving partial differential equations by using wavelet packet bases, *Comput. Meth. Appl. Mech. Eng.,* **116,** 301–307.

Kelly, K.R., Ward, R.W., Treitel, S. & Alford, R.M., 1976. Synthetic seismograms: a finite difference approach, *Geophysics,* **41,** 2–27.

Komatitsch, D. & Tromp, J., 1999. Introduction to the spectral element method for three-dimensional seismic wave propagation, *J. Sci. Comp.,* **139,** 806–822.

Kosloff, D. & Baysal, E., 1982. Forward modeling by a Fourier method, *Geophysics,* **47,** 1402–1412.

Lazaar, S., Liandrat, J. & Tchamitchian, P., 1994. Algorithmes à base d'ondelettes pour la résolution numériques d'équations aux dérivés partielles à coefficients variables, *C.R. Acad. Sci. Paris,* **319,** 1101–1107.

Levander, A.R., 1988. Fourth-order finite-difference *P–SV* seismograms, *Geophysics,* **53,** 1425–1436.

Magnier, S.A., Mora, P. & Tarantola, A., 1994. Finite differences on minimal grids, *Geophysics,* **59,** 1435–1443.

Mallat, S., 1989. Multiresolution approximation and wavelets, *Trans. Amer. Math. Soc.,* **315,** 69–88.

Mallat, S., 1999. *A Wavelet Tour of Signal Processing,* Academic Press, New York.

Mozco, P., Lucká, M., Kristek, J. & Kristeková, M., 1999. 3D displacement finite differences and a combined memory optimization, *Bull. seism. Soc. Am.,* **89,** 69–79.

Operto, S., Virieux, J., Malfanti, F. & Hustedt, B., 2000. Adaptive seismic wave modeling in wavelet bases, in *Proc. 5th Int. Conf. on Mathematical and Numerical Aspects of Wave Propagation,* pp. 858–862, SIAM-INRIA.

Pitarka, A., 1999. 3D elastic finite-difference modeling of seismic motion using staggered grids with nonuniform spacing, *Bull. seism. Soc. Am.,* **89,** 54–68.

Press, W.H., Teukolsky, S.A., Vetterling, W.T. & Flannery, B.P., 1992. *Numerical Recipes in Fortran 77, Second Edition, The Art of Scientific Computing*. Cambridge University Press, Cambridge.

Sambridge, M., Braun, J. & McQueen, H., 1995. Geophysical parametrization and interpolation of irregular data using natural neighbours, *J. Sci. Comp.,* **122,** 837–857.

Stekl, I. & Pratt, R.G., 1998. Accurate viscoelastic modeling by frequency-domain finite differences using rotated operators, *Geophysics,* **63,** 1779–1794.

Sweldens, W., 1997. The lifting scheme: a construction of second generation wavelets, *SIAM J. Math. Anal.,* **29,** 511–546.

Tessmer, E., 2000. Seismic finite-difference modeling with spatially varying time steps, *Geophysics,* **65,** 1290–1293.

Virieux, J., 1984. *SH* wave propagation in heterogeneous media, *Geophysics,* **49,** 1259–1266.

Wu, Y. & McMechan, G., 1998. Wave extrapolation in the spatial wavelet domain with application to postack reverse-time migration, *Geophysics,* **63,** 589–600.

Zhang, Y.-G. & Ballmann, J., 1997. Two techniques for the absorption of elastic waves using an artificial transition layer, *Wave Motion,* **25,** 15–33.

## APPENDIX A: DIFFERENTIAL OPERATOR IN THE WAVELET DOMAIN

The expression of a differential operator in the Daubechies wavelet basis has been proposed by Beylkin (1992).

The description of the algorithm will show the connection between the representation of the differential operator in wavelet basis and the finite-difference approximation of the differential operator at a given scale. Let us consider a function $f(x, z)$ defined in an infinite 2-D medium. The projection in $\mathbf{V}_0$ of the partial derivative with respect to the $x$ coordinate of $f$, denoted as $P_{\mathbf{V}_0}(f') = P_{\mathbf{V}_0}(\partial/\partial x)$, can be decomposed in the scaling function basis $\phi_0$ at that scale 0 as

$$P_{\mathbf{V}_0}(f') = \sum_{n=-\infty}^{+\infty} \langle f', \phi_{0,n}\rangle \phi_{0,n}\,. \tag{A1}$$

Integrating by parts $\langle f', \phi_{0,n}\rangle$ gives

$$P_{\mathbf{V}_0}(f') = -\sum_{n=-\infty}^{+\infty} \langle f, \phi'_{0,n}\rangle \phi_{0,n}\,, \tag{A2}$$

where partial derivative operations have moved to basis functions. Following standard operator calculus, we expand the function $f$ in the same scaling function basis as the partial derivative and find

$$\begin{aligned} P_{\mathbf{V}_0}(f') &= -\sum_{n=-\infty}^{+\infty}\sum_{m=-\infty}^{+\infty} \langle f, \phi_{0,m}\rangle\langle \phi_{0,m}, \phi'_{0,n}\rangle \phi_{0,n} \\ P_{\mathbf{V_0}}(f') &= -\sum_{n=-\infty}^{+\infty}\sum_{m=-\infty}^{+\infty} \langle f, \phi_{0,m}\rangle r_{m-n}\phi_{0,n}\,, \end{aligned} \tag{A3}$$

where only coefficients of the function $f$ are involved. The coupling coefficients $r_{m-n}$ between the two basis expansions are the elements of the differential operator matrix in the scaling function basis. Beylkin (1992) designed an algorithm to compute the coefficients $r_l$ efficiently for the Daubechies wavelet basis (see Proposition 1, p. 1721 in Beylkin 1992). The coefficients $r$ have two important properties:

(1) $r_l = -r_{-l}$;
(2) the number $l$ of non-zero coefficients $r$ is $2\,(2M-2)+1$

where $M$ is the number of vanishing moments of the wavelets. Therefore, the double summation over integers $n$ and $m$ will have few non-zero elements. Beylkin obtained the following coefficients $r_0 = 0$, $r_1 = -2/3$, $r_2 = 1/12$ for the Daubechies-4 wavelets. They turn out to be exactly the coefficients of the fourth-order finite-difference approximation of the differential operator for a given scale. This was also underlined by Jameson (1993).

We may perform the decomposition of the partial derivative operator of $f$ over subspaces $\mathbf{V}_1$ and $\mathbf{W}_1$. We obtain

$$\begin{aligned} P_{\mathbf{V}_0}(f') &= P_{V_0}\left(\frac{\partial}{\partial x} f\right) = P_{V_1 U W_1}\left(\frac{\partial}{\partial x} f\right) \\ &= \sum_{n=-\infty}^{+\infty} \langle f', \psi_{1,n}\rangle \psi_{1,n} + \sum_{n=-\infty}^{+\infty} \langle f', \phi_{1,n}\rangle \phi_{1,n} \\ &= \sum_{n=-\infty}^{+\infty} d'_1 \psi_{1,n} + \sum_{n=-\infty}^{+\infty} s'_1 \phi_{1,n}\,. \end{aligned} \tag{A4}$$

The coefficients $d'_1$ are the wavelet coefficients obtained by the orthogonal projection of the partial derivative of $f$, $f' = \frac{\partial}{\partial x} f$, on the subspace $\mathbf{W}_1$. Coefficients $s'_1$ are the scaling coefficients obtained by the orthogonal projection of $f'$ on the complementary subspace $\mathbf{V}_1$. They will be used for further estimations of wavelet coefficients of $f'$ at scales coarser than 1.

After the same straight recipe as for eq. (A3), we obtain an expression of the partial derivative operator with respect to the

coordinate $x$ using only coefficients of the function $f$,

$$P_{\mathbf{V}_0}(f') = -\sum_{n=-\infty}^{+\infty}\sum_{m=-\infty}^{+\infty} \langle f, \psi_{1,m}\rangle \alpha^1_{m,n}\psi_{1,n} - \sum_{n=-\infty}^{+\infty}\sum_{m=-\infty}^{+\infty} \langle f, \phi_{1,m}\rangle \beta^1_{m,n}\psi_{1,n} - \sum_{n=-\infty}^{+\infty}\sum_{m=-\infty}^{+\infty} \langle f, \psi_{1,m}\rangle \gamma^1_{m,n}\phi_{1,n} - \sum_{n=-\infty}^{+\infty}\sum_{m=-\infty}^{+\infty} \langle f, \phi_{1,m}\rangle r^1_{m,n}\phi_{1,n}\,, \tag{A5}$$

where $\alpha$, $\beta$, $\gamma$, $r$ coefficients and cross products of basis functions are denoted as

$$\alpha^1_{m,n} = \langle \psi_{1,m}, \psi'_{1,n}\rangle \tag{A6}$$

$$\beta^1_{m,n} = \langle \phi_{1,m}, \psi'_{1,n}\rangle \tag{A7}$$

$$\gamma^1_{m,n} = \langle \psi_{1,m}, \phi'_{1,n}\rangle \tag{A8}$$

$$r^1_{m,n} = \langle \phi_{1,m}, \phi'_{1,n}\rangle\,. \tag{A9}$$

We follow the notation proposed by Beylkin (1992) [see eqs (3.5)–(3.8) in Beylkin (1992)]. The coefficients $r^1_{m,n}$ represent the matrix elements of the differential operator in the subspace $\mathbf{V}_1$, namely, $\partial P_{\mathbf{V}_1}/\partial x$. From eqs (1) and (2) we see that the coefficients $\alpha^i_{m-n}$, $\beta^i_{m-n}$, $\gamma^i_{m-n}$ and $r^i_{m-n}$ are related to the coefficients $\alpha_{m-n}=\alpha^0_{m-n}$, $\beta_{m-n}=\beta^0_{m-n}$, $\gamma_{m-n}=\gamma^0_{m-n}$ and $r_{m-n}=r^0_{m-n}$ by a scaling coefficient of $2^{-j}$, respectively (Beylkin 1992). We may conclude that the expression of the partial derivative operator in the subdomain $\mathbf{V}_1$ is similar to the fourth-order finite-difference operator at that scale, as was already noted in the domain $\mathbf{V}_0$.

Moreover, the coefficients $\alpha_{m-n}$, $\beta_{m-n}$ and $\gamma_{m-n}$ can be derived from the tabulated coefficients $r_{m-n}$ and the coefficients of the quadrature mirror filters [see eq. (3) and the original equations (3.13) and (3.14) in Beylkin (1992)].

Consequently, the discretized differential operator in any subspace $\mathbf{V}_i$ can be derived very efficiently from the discretized form of the differential operator in the discretized grid of the domain $\mathbf{V}_0$.

Eq. (A5) which relates the wavelet coefficients $d'$ and $s'$ to the wavelet coefficients $d$ and $s$ of the function $f$ can be written in matrix form as

$$\begin{aligned} d'_1 &= A_1 d_1 + B_1 s_1 \\ s'_1 &= \Gamma_1 d_1 + R_1 s_1\,, \end{aligned} \tag{A10}$$

where matrices $A_1$, $B_1$, $\Gamma_1$ and $R_1$ are computed before any numerical simulation starts (Fig. A1a).

In order to see the coupling between scales, we continue the wavelet decomposition. We shall now decompose the $s'_1$ coefficients into a pair of coefficients $d'_2$ and $s'_2$. Following the hierarchical scheme of Fig. A1(b), we transform the system (A10) into the following recursive system:

$$\begin{aligned} d'_1 &= A_1 d_1 + B_{1d} d_2 + B_{1s} s_2 \\ d'_2 &= \Gamma_{1d} d_1 + A_2 d_2 + B_2 s_2 \\ s'_2 &= \Gamma_{1s} d_1 + \Gamma_2 d_2 + R_2 s_2\,. \end{aligned} \tag{A11}$$

We may decompose this estimation into three steps.

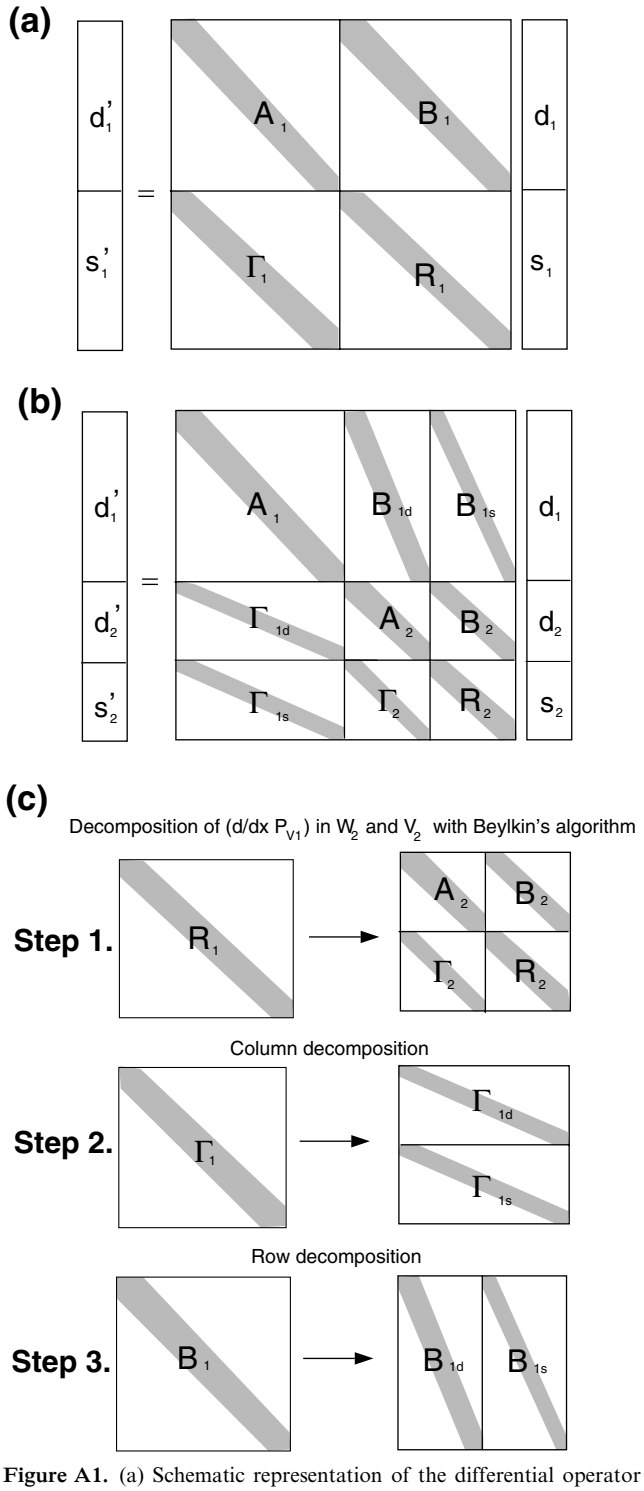


**Figure A1.** (a) Schematic representation of the differential operator in the wavelet basis with one multiresolution level. (b) Schematic representation of the differential operator in the wavelet basis with two multiresolution levels. (c) Sketch of the three-step procedure allowing the computation of the matrix in Figure A1(b) from Figure A1(a).

(1) As for the scaling level 1 of the multiresolution analysis, the matrices $A_2$, $B_2$, $\Gamma_2$ and $R_2$ can be derived efficiently from coefficients $r$ using the algorithm of Beylkin (step 1 in Fig. A1c).

(2) The coupling matrices $\Gamma_{1d}$ and $\Gamma_{1s}$ are computed by applying a wavelet decomposition to each column of the matrix $\Gamma_1$ (step 2 in Fig. 5c) as shown by a wavelet decomposition of

the second equation of the system (A10). The wavelet transform operator $C$ gives

$$C\,s_1' = [C\,\Gamma_1]\,d_1 + [C\,R_1\,C^t]\,[C\,s_1] \tag{A12}$$

which performs the wavelet decomposition of coefficient $s_1'$ into $s_2'$, $d_2'$ and $s_1$ into $s_2$, $d_2$. The matrix multiplication $[C\,\Gamma_1]$ is equivalent to the wavelet decomposition of each column of the matrix $\Gamma_1$. Let us recall that the term $[C\,R_1\,C^t][C\,s_1]$ has been evaluated by the first step of Beylkin's algorithm.

(3) The matrices $B_{1d}$ and $B_{1s}$ are computed by applying a wavelet decomposition to each row of the matrix $B_1$ (step 3 in Fig. A1c). Indeed, the coefficient $d_1' = A_1\,d_1 + B_1\,s_1$ can be rewritten as $d_1' = A_1\,d_1 + [B_1\,C^t][C\,s_1]$, where $C\,s_1$ is the decomposition of coefficient $s_1$ into $d_2$, $s_2$.

The three-step procedure can be cascaded down to any *a priori* subspace $\mathbf{V}_J$ at scale $J$. These estimations can be performed once and stored before any wave propagation simulation starts.

The partial differential operator in the Daubeschies-4 wavelet basis corresponding to the example of Fig. 1 is shown in Fig. A2. The matrix is band-diagonal with fringes. The fringes illustrate the coupling between scales. This coupling appeared in the wavelet decomposition during the computation of the second and third step of the algorithm. Note that the coefficients of the band diagonal are the coefficients of the fourth-order finite-difference approximation of the differential operator scaled by $2^j$. Therefore, the band diagonal coefficients decrease from fine to coarser scales. The amplitude of the fringe coefficients decrease for either horizontal or vertical scales as we move away from the diagonal. This illustrates the intuitive idea that the greater the difference in resolution of the scales, the weaker the coupling between them.

Although the introduction of scales makes the notation more cumbersome, the different matrices that turn out to be sparse can be tabulated *a priori* before starting the time extrapolation. During simulation we certainly require efficient matrix–vector and matrix–matrix products as we shall see.

## APPENDIX B: DERIVATION OF EQ. (8)

We derive eq. (8) which is denoted below as

$$\left\langle g(x,z)\,\frac{\partial f(x,z,t)}{\partial x},\,\Psi_i(x)\Psi_l(z)\right\rangle = -\sum_j\sum_k\left\langle \Psi_j(x),\,\frac{\partial\Psi_k(x)}{\partial x}\right\rangle \sum_m \langle f(x,z,t),\,\Psi_j(x)\Psi_m(z)\rangle \times\langle\Psi_k(x)\Psi_m(z),\,g(x,z)\Psi_i(x)\Psi_l(z)\rangle\,. \tag{B1}$$

The wavelet coefficient of index $i$ is given by $\langle g(x,z)\partial f(x,z,t)/\partial x,\,\Psi_i(x)\rangle$. By permutation, we obtain

$$\left\langle g(x,z)\,\frac{\partial f(x,z,t)}{\partial x},\,\Psi_i(x)\right\rangle = \left\langle g(x,z)\Psi_i(x),\,\frac{\partial f(x,z,t)}{\partial x}\right\rangle. \tag{B2}$$

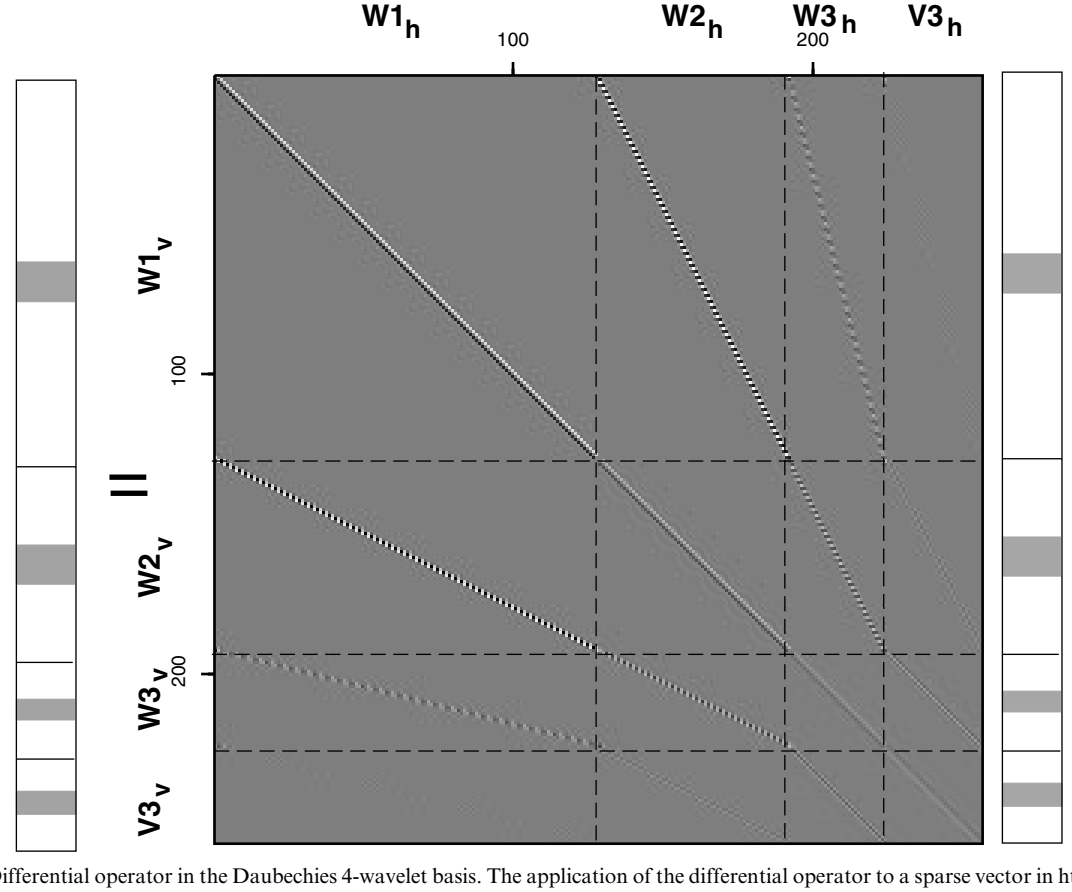


**Figure A2.** Differential operator in the Daubechies 4-wavelet basis. The application of the differential operator to a sparse vector in hte wavelet basis is illustrated. The sparsity of the output vector is preserved after a matrix–vector product.

Using a similar procedure to previously, we expand the expression $\partial f(x, z, t)/\partial x$ on to a new wavelet basis that gives

$$\left\langle g(x, z)\Psi_i(x), \frac{\partial f(x, z, t)}{\partial x}\right\rangle = \sum_j \langle g(x, z)\Psi_i(x), \Psi_j(x)\rangle \left\langle \Psi_j(x), \frac{\partial f(x, z, t)}{\partial x}\right\rangle \quad \text{(B3)}$$

which can be integrated by parts. Because wavelets have local supports, one can show that

$$\left\langle \Psi_j(x), \frac{\partial f(x, z, t)}{\partial x}\right\rangle = -\left\langle \frac{\partial \Psi_j(x)}{\partial x}, f(x, z, t)\right\rangle. \quad \text{(B4)}$$

Again, one can project $\partial\Psi_j(x)/\partial x$ on to a new wavelet basis giving a new expression of the product

$$-\left\langle \frac{\partial \Psi_j(x)}{\partial x}, f(x, z, t)\right\rangle = -\sum_m \left\langle \frac{\partial \Psi_j(x)}{\partial x}, \Psi_k(x)\right\rangle \langle \Psi_k(x), f(x, z, t)\rangle. \quad \text{(B5)}$$

Finally, the wavelet transform with respect to the $x$ coordinate of $g(x, z)\partial f(x, z, t)/\partial x$ can be factorized as

$$\left\langle g(x, z)\frac{\partial f(x, z, t)}{\partial x}, \Psi_i(x)\right\rangle = -\sum_j \langle g(x, z)\Psi_i(x), \Psi_j(x)\rangle \times \sum_k \left\langle \frac{\partial \Psi_j(x)}{\partial x}, \Psi_k(x)\right\rangle \langle \Psi_k(x), f(x, z, t)\rangle. \quad \text{(B6)}$$

Now, we project equation (B6) on to a 1-D wavelet basis with respect to the $z$ coordinate. The 2-D wavelet coefficient of index $(i, l)$ can be expressed as

$$\left\langle g(x, z)\frac{\partial f(x, z, t)}{\partial x}, \Psi_i(x)\Psi_l(z)\right\rangle = -\sum_j \sum_k \left\langle \frac{\partial \Psi_j(x)}{\partial x}, \Psi_k(x)\right\rangle \times \langle\langle g(x, z)\Psi_i(x), \Psi_j(x)\rangle\langle \Psi_k(x), f(x, z, t)\rangle, \Psi_l(z)\rangle \quad \text{(B7)}$$

which is equivalent to

$$\left\langle g(x, z)\frac{\partial f(x, z, t)}{\partial x}, \Psi_i(x)\Psi_l(z)\right\rangle = -\sum_j \sum_k \left\langle \frac{\partial \Psi_j(x)}{\partial x}, \Psi_k(x)\right\rangle \times \langle\langle g(x, z)\Psi_i(x)\Psi_l(z), \Psi_k(x)\rangle, \langle \Psi_k(x), f(x, z, t)\rangle\rangle. \quad \text{(B8)}$$

Projection on to a new wavelet basis with respect to $z$ gives the final expression

$$\left\langle g(x, z)\frac{\partial f(x, z, t)}{\partial x}, \Psi_i(x)\Psi_l(z)\right\rangle = -\sum_j \sum_k \left\langle \frac{\partial \Psi_j(x)}{\partial x}, \Psi_k(x)\right\rangle \times \sum_m \langle g(x, z)\Psi_i(x)\Psi_l(z), \Psi_k(x)\Psi_m(z)\rangle \times \langle \Psi_k(x)\Psi_m(z), f(x, z, t)\rangle \quad \text{(B9)}$$

which concludes the derivation of eq. (B1).

## APPENDIX C: PML ABSORBING BOUNDARY CONDITIONS IN THE WAVELET DOMAIN

To match the PML condition the hyperbolic system in eq. (9) must be rewritten (Berenger 1994; Zhang & Ballmann 1997):

$$\begin{cases} \dfrac{\partial v_{xy}(x, z, t)}{\partial t} + \sigma_x(x)v_{xy}(x, z, t) \\ \quad = b(x, z)\,\frac{\partial \tau_{xy}(x, z, t)}{\partial x} + f(x, z, t) \\ \dfrac{\partial v_{zy}(x, z, t)}{\partial t} + \sigma_z(z)v_{zy}(x, z, t) = b(x, z)\,\dfrac{\partial \tau_{zy}(x, z, t)}{\partial z} \\ \dfrac{\partial \tau_{xy}(x, z, t)}{\partial t} + \sigma_x(x)\tau_{xy}(x, z, t) = \mu(x, z)\,\dfrac{\partial v_y(x, z, t)}{\partial x} \\ \dfrac{\partial \tau_{zy}(x, z, t)}{\partial t} + \sigma_z(z)\tau_{zy}(x, z, t) = \mu(x, z)\,\dfrac{\partial v_y(x, z, t)}{\partial z}, \end{cases} \quad \text{(C1)}$$

where $v_y(x, z, t) = v_{xy}(x, z, t) + v_{zy}(x, z, t)$.

$\sigma_x(x)$ and $\sigma_z(z)$ are the damping factors of the PML media. Their values are 0 inside the medium and increase from 0 to $\sigma_{\max}$ when going from the medium–PML interface to the outer limit of the PML. Berenger (1994) showed that the reflection coefficient at a PML–PML interface (including the medium–PML interface) is zero theoretically for the system (C1). Then, $\sigma$ can be designed such that waves are rapidly damped in the absorbing layers.

The system is discretized with respect to time using a centred finite-difference scheme:

$$\begin{cases} \dfrac{v_{xy}^{n+1/2}(x, z) - v_{xy}^{n-1/2}(x, z)}{\Delta t} + 1/2\sigma_x(x)\left[v_{xy}^{n+1/2}(x, z) + v_{xy}^{n-1/2}(x, z)\right] \\ \quad = b(x, z)\dfrac{\partial \tau_{xy}^n(x, z)}{\partial x} + f^n(x, z) \\ \qquad \times \dfrac{v_{zy}^{n+1/2}(x, z) - v_{zy}^{n-1/2}(x, z)}{\Delta t} \\ \qquad +1/2\sigma_z(z)\left[v_{zy}^{n+1/2}(x, z) + v_{zy}^{n-1/2}(x, z)\right] \\ \quad = b(x, z)\dfrac{\partial \tau_{zy}^n(x, z)}{\partial z} \\ \qquad \times \dfrac{\tau_{xy}^{n+1}(x, z) - \tau_{xy}^n(x, z)}{\Delta t} \\ \qquad +1/2\sigma_x(x)\left[\tau_{xy}^{n+1}(x, z) + \tau_{xy}^n(x, z)\right] \\ \quad = \mu(x, z)\dfrac{\partial v_y^{n+1/2}(x, z)}{\partial x} \\ \qquad \times \dfrac{\tau_{zy}^{n+1}(x, z) - \tau_{zy}^n(x, z)}{\Delta t} \\ \qquad +1/2\sigma_z(z)\left[\tau_{zy}^{n+1}(x, z) + \tau_{zy}^n(x, z)\right] = \mu(x, z)\dfrac{\partial v_y^{n+1/2}(x, z)}{\partial z}. \end{cases} \quad \text{(C2)}$$

Regrouping terms with respect to the time index and approximating $1 \pm \Delta t\, \sigma_x/2$ by $e^{\pm \Delta t \sigma_x/2}$ give

$$\begin{cases} v_{xy}^{n+1/2}(x,z) = e^{-\Delta t \sigma_x(x)} v_{xy}^{n-1/2}(x,z) + e^{-\Delta t \sigma_x(x)/2} \Delta t b(x,z) \dfrac{\partial \tau_{xy}^{n}(x,z)}{\partial x} \\ \qquad\qquad + \Delta t\, e^{-\Delta t \sigma_x/2(x)} f^n(x,z) \\ v_{zy}^{n+1/2}(x,z) = e^{-\Delta t \sigma_x(x)} v_{zy}^{n-1/2}(x,z) + e^{-\Delta t \sigma_x(x)/2} \Delta t b(x,z) \dfrac{\partial \tau_{zy}^{n}(x,z)}{\partial z} \\ \tau_{xy}^{n+1}(x,z) = e^{-\Delta t \sigma_x(x)} \tau_{xy}^{n}(x,z) + e^{-\Delta t \sigma_x(x)/2} \Delta t \mu(x,z) \dfrac{\partial v_y^{n+1/2}(x,z)}{\partial x} \\ \tau_{zy}^{n+1}(x,z) = e^{\Delta t \sigma_x(x)} \tau_{zy}^{n}(x,z) + e^{-\Delta t \sigma_x(x)/2} \Delta t \mu(x,z) \dfrac{\partial v_y^{n+1/2}(x,z)}{\partial z}\,. \end{cases} \tag{C2}$$

This system shows that the PML absorbing condition is equivalent to the sponge-like absorbing boundary condition of Cerjan *et al.* (1985), except that $v_y$ is first split on to $v_{xy}$, and $v_{zy}$ and the horizontal and vertical damping $\sigma_x$ and $\sigma_z$ are only applied to $v_{xy}$ and $v_{zy}$, respectively.

In matrix form, the damping terms $e^{-\Delta t\, \sigma_x(x)/2}$ can be described as a diagonal operator $\mathscr{D}_a$. Inside the medium the diagonal elements are equal to 1 and decrease progressively from 1 at the medium–PML interface to a minimum value at the outer limit of the PML. The wavelet coefficients of this operator after projection on to a 1-D wavelet basis are given by $\langle \mathscr{D}_a \Psi_\alpha, \Psi_\beta \rangle$, where $\alpha$ and $\beta$ are all possible pairs of wavelet indices of the discrete basis. Wu & McMechan (1998) showed that the off-diagonal coefficients of the matrix can be considered to be negligible when using the absorbing condition of Cerjan *et al.* (1985) in the wavelet domain. This allows fast implementations of the absorbing boundary condition. We used an absorbing layer of thickness around four wavelengths. In equation C2, we replace the function $e^{-\Delta t \sigma_x(x)/2}$ by a function of the form $\cos(ax)$ in the absorbing layer. $a$ was chosen such that the value of $\sigma$ at the outer limit of the absorbing layer gave 0.88, which gave the best results. Note that the 0.88 damping coefficient for the PML absorbing condition is slighty higher than that used in Cerjan *et al.* (1985) (0.92). It confirms that PML performs damping of waves in the absorbing medium more efficiently.